1.1 Introduction

Topological insulators (TI), which are insulating in bulk but conducting at the surfaces, are emerging materials attracting a large interest in the area of condensed matter physics. The topological property of materials is due to gapless edge or spin resolved surface states (SS), topologically protected by time reversal symmetry (TRS). The spins are locked in the perpendicular direction of momentum due to the strong spin-orbit interaction. As a matter of fact, electrical conduction is robust against backscattering at the edge states or on the surfaces in TIs. These special helical spin properties of electrons make TIs interesting and relevant for new physics. Since the locking of spin and orbital states is protected by time reversal symmetry, the delocalized surface states are unaffected from nonmagnetic dopant and defects [1, 2]. Moreover the coupling of the spin and orbital angular momentum of an electron leads to an inversion of the band gap. The existence of exotic properties, such as, the possibility of Majorana Fermions, topological superconductivity, novel magnetoelectric quantum states, absence of backscattering from nonmagnetic impurities, exciton condensation, magnetic monopole, and anomalous quantum Hall effect in TIs are very promising for application in spintronics devices and quantum computing [1, 2]. Topological surface states in Bi_2Te_3 and Bi_2Se_3 with only one mass less Dirac cone on each surface were studied using Angle-resolved photoemission spectroscopy (ARPES) [1]. Quantum magneto-transport phenomenon such as weak antilocalization, Aharonov-Bohm oscillations and quantum conductance fluctuations are associated with surface states [1, 2]. It has been theoretically predicted that surface state of a topological insulator shows a linear energy-momentum relation similar to Dirac fermions. The time reversal symmetry protection of the Dirac point can be lifted by magnetic dopant, resulting in a band gap due to the separation in

the upper and lower branches of the Dirac cone [1, 2]. Both two and three dimensional topological insulator materials have been theoretically predicted [3] and also experimentally obtained [4, 5]. In this chapter, an overview of some of the essential properties of these new types of materials has been discussed.

To understand topological insulators, it is important to discuss band theory of solids, which is the underlying physics for determining the insulating property of a material.

1.1.1Band Theory of Solids

The material is metal; insulator or semiconductor is decided by band theory of solids in condensed matter physics. The simple picture of band diagram has been shown in Fig.1.1 where lower energy state is valence band, upper energy state is conduction band and the distance between the valence band and the conduction band is called as band gap (shown in Fig.1.1). The band gap represents the minimum energy which is required to excite an electron up from valence band to the conduction band so that it can participate in conduction. The size of the band gap determines whether a material is conductor, semiconductor or insulator.

In conductors, the conduction band overlaps with the valence band which causes the valence electrons to move freely into the conduction band and participate in conduction. But, since, it is not a full overlap, hence only a fraction of the valence electrons can move through the material, although this is still enough to make the material conductive. In insulators, the valence band is separated by a large band gap from the conduction band which may be of the order of >5eV. Due to such a large gap, the thermal energy at 300K (~25 meV) is insufficient to excite electrons from the valence band to the conduction band such that the valence band

is fully occupied whereas the conduction band is empty. Thus, in insulator, large "forbidden" gap prevents electrons to participate in conduction.

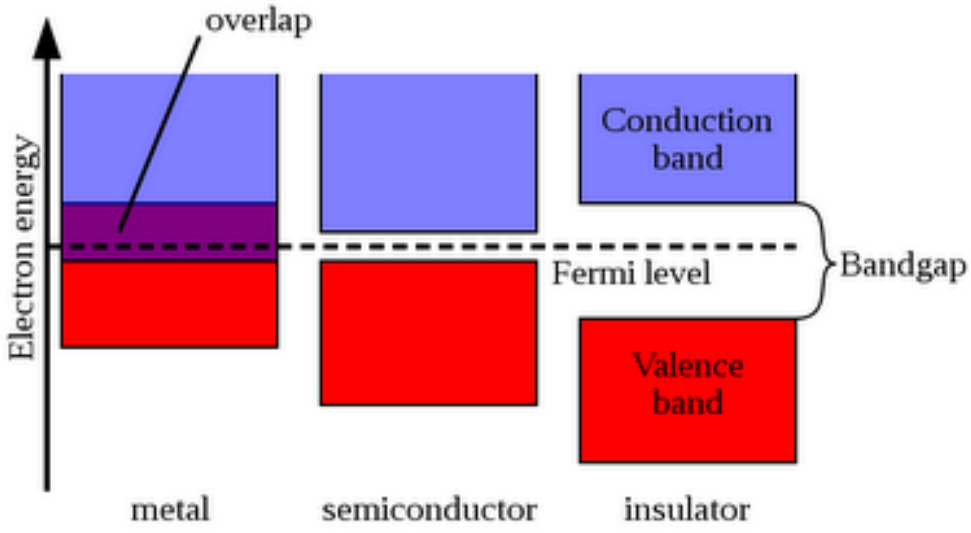

Fig.1.1 Schematic band diagram for metal, semiconductor and insulator

Semiconductors are the materials whose electronic properties are intermediate of the conductors and insulators. The band gap of semiconductor is small but non-zero (~1 eV); they behave as an insulator at absolute zero, but allow thermal excitation of electrons from the valence band into its conduction band at temperatures which is below its melting point. Unlike conductor, semiconductor has both positive (hole) and negative (electrons) carriers of electricity whose densities can be controlled by doping during crystal growth. Even small amount of dopant can drastically increase the conductivity of a semiconductor material.

1.1.2 What is topology?

Topology is a branch of mathematics in which the properties of object which are invariant under smooth deformation are studied. Coffee cup and donut is a classic example of

topology. In Fig.1.2 (a), it is shown that coffee cup is changing its shape in to donut with a continuous deformation. If we integrate the local curvature R over the entire space, it gives

$$\frac{1}{2\pi}\int R\, dS = 2 - 2g \qquad (1.1)$$

(a) **(b)** **(c)**

Fig.1.2 (a) Schematic representation of topology showing smooth deformation from cup to donut (b) Sphere showing different topology than cup and donut (c) Effect of external parameter on topology of donut.

Here 'g' stands for the genus which, in the above Fig. 1.2, is equivalent to the number of holes. In the case of coffee cup and donut [shown in Fig.1.2(a)], the number of holes is same and is equal to 1, hence we can say that both have the same topological class, but for sphere [shown in Fig. 1.2(b)] g = 0 since it does not contain any hole, hence sphere and donut have different classes of topology. It is also clear from the above discussion that if we do not disturb the number of holes, topology of the objects remains same. Similar phenomenon happens in the case of topological insulators where its topological properties are governed by some topological invariants and if no change occurs in those invariants, the material retain their topological properties and those invariant are analogous to genus 'g' as described above. In Fig. 1.2(c) there is some external cut on the donut, but there is no change in the number of hole hence topology of the donut remains same. In the same manner, topological

surface states are robust against doping and external environmental disturbance until it affects the topological invariants.

We can define a Berry curvature in the Brillion zone instead of a Gaussian curvature defined above in equation (1.1). The surface integral of Berry flux 'F' in terms of vector potential 'A' may be expressed as,

$$F = (\nabla_k \times \boldsymbol{A})z \tag{1.2}$$

The Chern invariant in TIs can be understood physically in terms of Berry phase which is associated with the Bloch wave functions $|u_m(k)>$, where k represents the momentum. When k is transported around a closed loop $|u_m(k)>$, it gets a Berry phase which may be expressed by the line integral

$$A_m = i < u_m|\nabla_k |u_m> \tag{1.3}$$

It may be expressed as surface integral of Berry flux

$$F_m = \nabla \times A_m \tag{1.4}$$

The total Berry flux in the Brillion zone is the Chern invariant and may be expressed as

$$n_m = \frac{1}{2\pi}\int d^2k\, F_m \tag{1.5}$$

Here n_m is the quantized integer called as a Chern number [1] when the Hamiltonian varies smoothly; the Chern number n is a topological invariant.

Hasan and Kane [1] have mentioned that an insulator is trivial if n=0 and it is quantum spin Hall insulator if n=1. A trivial insulator has gapped edge, while a quantum spin Hall insulator has a pair of gapless helical edge states, carrying the electrons having opposite

spins, therefore the edge is conducting unlike the trivial insulators. Moreover, in 3D topological insulator, electric magnetic response can be expressed by the topological θ term having the form

$$S_\theta = \frac{\theta}{2\pi}\frac{\alpha}{2\pi\alpha}\int d^3x\, dt\, \boldsymbol{E}.\boldsymbol{B} \qquad (1.6)$$

α is the fine structure constant, **E** and **B** are the electromagnetic field. If θ=0, it will show conventional insulators but if θ=π, it will represent topological insulators [6].

1.1.3 Interesting features of Topological Insulators

In daily life, we break the symmetry generally to make the system more interesting and exotic, for example, in liquid crystals there is breaking of translational symmetry, in ferromagnetic materials, rotational symmetry breaks and in superconductors, there is breaking of gauge symmetry but the surprising and interesting point in topological insulators is that, the beauty of material is due to preservation of symmetry. The topological surface state (TSS) always preserves time reversal symmetry (TRS).

1.1.4 Time Reversal Symmetry

The Hamilton operator can be given as (1.7)

$$H = \frac{\mathbf{p}^2}{2m} + \mathrm{V}(\mathbf{r}) + \frac{\mu_B}{\hbar}(\mathbf{L} + 2\mathbf{S})\mathbf{B} \qquad (1.7)$$

Where p is the momentum, m is the mass of electron, V(r) is the potential, μ_B is the Bohr magnetron, L and S are is angular and spin momentum respectively.

Now, Pauli-Schrodinger equation can be represented as

$$i\hbar\partial_t\psi(\mathbf{r},t) = \left[-\frac{\hbar^2}{2m}\Delta + \mathrm{V}(\mathbf{r}) + \frac{\mu_B}{\hbar}(\mathbf{L} + 2\mathbf{S})\mathbf{B}\right]\psi(\mathbf{r},t) \qquad (1.8)$$

Time-reversed magnetic field: $\mathbf{B}' = -\mathbf{B}$
Time-reversed Pauli-Schrodinger equation can be given as

$$-i\hbar\partial_t\psi'(\mathbf{r},Tt) = \left[-\frac{\hbar^2}{2m}\Delta + \mathrm{V}(\mathbf{r}) + \frac{\mu_B}{\hbar}(\mathbf{L}+2\mathbf{S})\mathbf{B}'\right]\psi'(\mathbf{r},Tt) \quad (1.9)$$

$$= \left[-\frac{\hbar^2}{2m}\Delta + \mathrm{V}(\mathbf{r}) + \frac{\mu_B}{\hbar}(\mathbf{L}+2\mathbf{S})\mathbf{B}\right]\psi'(\mathbf{r},Tt) \quad (1.10)$$

Moreover,

$$-i\hbar\partial_t\psi^*(\mathbf{r},t) = \left[-\frac{\hbar^2}{2m}\Delta + \mathrm{V}(\mathbf{r}) + \frac{\mu_B}{\hbar}(\mathbf{L}^*+2\mathbf{S}^*)\mathbf{B}\right]\psi^*(\mathbf{r},t) \quad (1.11)$$

$$= \left[-\frac{\hbar^2}{2m}\Delta + \mathrm{V}(\mathbf{r}) - \frac{\mu_B}{\hbar}(\mathbf{L}-2\mathbf{S}^*)\mathbf{B}\right]\psi^*(\mathbf{r},t) \quad (1.12)$$

$$\psi'(\mathbf{r},Tt) = \mathcal{L}\psi^*(\mathbf{r},t) = \mathcal{L}C\psi(\mathbf{r},t) \quad (1.13)$$

$$-i\hbar\mathcal{L}\partial_t\psi^*(\mathbf{r},t) = \left[-\frac{\hbar^2}{2m}\Delta + \mathrm{V}(\mathbf{r}) - \frac{\mu_B}{\hbar}(\mathbf{L}+2\mathbf{S})\mathbf{B}\right]\mathcal{L}\psi^*(\mathbf{r},t) \quad (1.14)$$

$$-i\hbar\partial_t\psi^*(\mathbf{r},t) = \left[-\frac{\hbar^2}{2m}\Delta + \mathrm{V}(\mathbf{r}) - \frac{\mu_B}{\hbar}(\mathbf{L}+2\mathcal{L}^{-1}\mathbf{S}\mathcal{L})\mathbf{B}\right]\mathcal{L}\psi^*(\mathbf{r},t) \quad (1.15)$$

This equation is satisfied only if

$$\mathcal{L}^{-1}\mathbf{S}\mathcal{L} = -\mathbf{S}^* = C\mathbf{S}C \Rightarrow \mathbf{S}\mathcal{L}C = -\mathcal{L}C\mathbf{S} \quad (1.16)$$

Let's use the notation: $T = \mathcal{L}C$

$$T\mathbf{S} = -\mathbf{S}T \quad (1.17)$$

But

$$T = \sigma_y C \quad (1.18)$$

is a satisfactory choice

Proof of Eq. (1.17) may be given by

$$\sigma_x^* = \begin{pmatrix}0 & 1\\ 1 & 0\end{pmatrix} = \sigma_x\sigma_y^* = \begin{pmatrix}0 & i\\ -i & 0\end{pmatrix} = -\sigma_y\sigma_z^* = \begin{pmatrix}1 & 0\\ 0 & -1\end{pmatrix} = \sigma_z \quad (1.19)$$

$$T^{-1}\sigma_x T = (-\sigma_y C)\sigma_x(\sigma_y C) = \sigma_y\sigma_x\sigma_y = -\sigma_x \quad (1.20)$$

$$T^{-1}\sigma_y T = (-\sigma_y C)\sigma_y(\sigma_y C) = -\sigma_y \quad (1.21)$$

$$T^{-1}\sigma_z T = (-\sigma_y C)\sigma_z(\sigma_y C) = \sigma_y\sigma_z\sigma_y = -\sigma_z \quad (1.22)$$

Properties:

$$T^{-1} = C\sigma_y = \sigma_y^* C = -\sigma_y C = -T \quad (1.23)$$

$$T^2 = -1 \tag{1.24}$$

From the relationship

$$\langle \psi | T\varphi \rangle = \langle \psi | \sigma_y C\varphi \rangle = \langle \sigma_y \psi | C\varphi \rangle = \left(\sigma_y^{rs}\right)^* \langle \psi_s | C\varphi_r \rangle = \langle \varphi_r | C\sigma_y^{rs}\psi_s \rangle$$
$$= \langle \varphi | C\sigma_y \psi \rangle = \langle \varphi | T\psi \rangle \tag{1.25}$$

it follows that

$$\langle \psi | T\psi \rangle = -\langle \psi | T\psi \rangle = 0 \tag{1.26}$$

Hence it is clear that ψ and Tψ is orthogonal to each other and, also, T is norm-conserving,

$$\langle T\psi | T\psi \rangle = -\langle \psi | T^2\psi \rangle = \langle \psi | \psi \rangle \tag{1.27}$$

The operator of spin-orbit coupling, $\frac{\hbar}{4m^2c^2}(\nabla V \times \mathbf{p})\sigma$, commutes with T

$$T^{-1}(\nabla V \times \mathbf{p})\sigma T = (T^{-1}(\nabla V \times \mathbf{p})T)(T^{-1}\sigma T)$$
$$= (\nabla V \times (-\mathbf{p}))(-\sigma) = (\nabla V \times \mathbf{p})\sigma \tag{1.28}$$

1.2 Effect of Magnetic Field in Different Type of Systems

In this section we will discuss about the different phenomenon produced due to the application of magnetic field on the various systems, along with this, we will also discuss the theory behind the discovery of topological insulators.

1.2.1 Hall Effect

The discovery of a topological insulator in condensed matter physics started with the discovery of Hall effects. In 1879, Edwin Hall discovered the Hall Effect. Consider a conductor in which electrical current is flowing. When magnetic field is applied in a direction perpendicular to the flow of the electric current, the charge carriers experience a force so called Lorentz force, in addition to the already existing electric field force. As a result, equal and opposite charges accumulate on the opposite faces, the separation of charge establishes an electric field which opposes the further migration of charge and hence a steady

electric potential is established for as long as the charge is flowing. This phenomenon is known as the Hall Effect and the generated voltage across the conductor is called as Hall voltage. The type of charge carriers (electrons or holes) as well as the density of carriers can be determined by studying Hall Effect.

Considering an n-type semiconductor (shown in Fig. 1.3), where the majority of charge carriers are electrons, such that the direction of the conventional current will be from left to right. If 'v' be the velocity of the electrons in the perpendicular direction of magnetic field then the magnitude of Lorentz force will be evB, where 'e' is the charge of elementary electron and B is the applied magnetic field in the z- direction. This causes the electrons to be deflected in the downward direction and hence negative charges accumulate on the bottom face of the conductor. Hence, a potential difference is developed between top and bottom surface with bottom face negative such that an electric field E_H is generated in the negative y direction. As a matter of fact a force eE_H acts in the upward direction on the electron. In the condition of equilibrium

$$eE_H=evB \qquad (1.29)$$

$$E_H=vB \qquad (1.30)$$

If the direction of current density (J_x) is in the x direction, then

$$J_x=nev \qquad (1.31)$$

Where n is the carrier concentration, hence

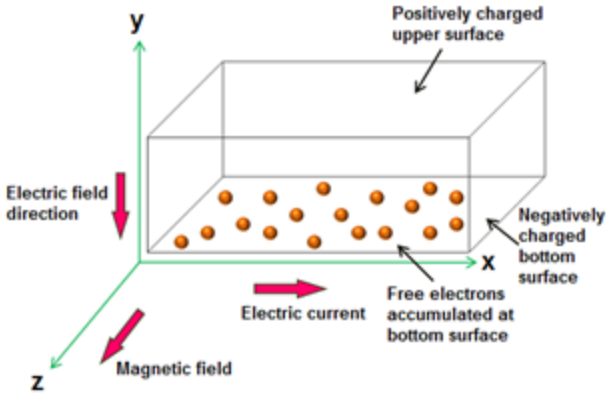

Fig.1.3 Schematic diagram of Hall Effect (Adopted from http://www.physics-and-radioelectronics.com /electronic-devices-and-circuits/semiconductor/halleffect.html).

$$E_{H=}\frac{BJ_x}{ne} \qquad (1.32)$$

The Hall coefficient R_H is defined as

$$E_H=R_HBJ_x \qquad (1.33)$$

Therefore,

$$R_{H=}\frac{E_H}{BJ_x} \qquad (1.34)$$

i.e. $$R_{H=}\frac{1}{ne} \qquad (1.35)$$

here it is:

$$R_{H=}-\frac{1}{ne} \qquad (1.36)$$

We have used negative sign because the development of electric field is in negative y – direction and hence we can say that if the sample is n-type i.e. carriers are electrons then,

$$R_{H=} -\frac{E_H}{BJ_x} = -\frac{1}{ne} \quad (1.37)$$

And if the sample is p-type i.e. current is entirely by holes then

$$R_{H=}\frac{E_H}{BJ_x} = \frac{1}{pe} \quad (1.38)$$

Here, n and p are the carrier concentration of the negative electrons and positive holes respectively. Hence using the Hall data we can determine the sign of carriers as well as carrier concentration. We can also determine the carrier mobility using Hall experiment. The mobility of electrons (μ_e) can be determined using the relation

$$\sigma = ne\mu_e \quad (1.39)$$

Here, σ is the conductivity of the material. In the same way, the mobility of holes (μ_p) can be given by the relation

$$\sigma = ne\mu_p \quad (1.40)$$

Here, we have discussed the effect of low magnetic field in 3D system but what was really surprising to physicists was the effect of high magnetic field in low dimension (2D) materials i.e. discovery of Integer Quantum Hall Effects (IQHE) in 1980. But before the discussion on the quantum Hall effect, it is necessary to discuss about the behavior of materials in the presence of high magnetic field.

1.2.2 Effect of Magnetic field in 3D System

It is observed that the application of high magnetic field produces many interesting phenomenon such as collapse of different energy levels in Landau levels, oscillations in the electrical resistivity with the variation of applied magnetic field (Shubnikov–de Haas effect),

oscillations of the magnetization as a function of applied magnetic field (de Haas-van Alfen effect) etc. Quantization of the energy of the conduction electrons in presence of high magnetic field is the reason behind the oscillations. Let B_Z is the applied field along the z direction, since magnetic field cannot exert force on the electrons moving in the direction of the magnetic field, hence there will be no effect on the motion of electrons in the z- direction. In such type of system, according to the quantum harmonic oscillator model, electrons behave as if they were free in the z- direction, but the motion of electrons is quantized in the x and y directions (Fig.1.4). The energy of such electrons can be expressed as [8].

$$E_n = \left(n + \frac{1}{2}\right)\hbar\omega_c + \frac{\hbar^2 k_z^2}{2m_e^*} \quad \text{Where n=0, 1, 2, 3} \qquad (1.41)$$

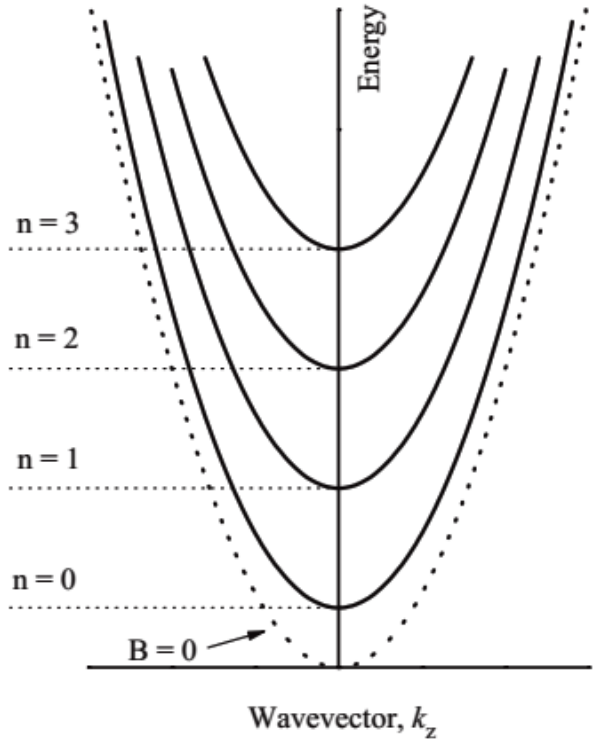

Fig.1.4 Energy band diagram for electrons vs. wave vector for different Landau levels in 3D system [8].

Here, quantum number n corresponds to different Landau levels and k_z is the momentum of electron in z- direction, m_e^* is the effective mass of electron and ω_c is the cyclotron frequency represented as

$$\omega_c = \frac{eB_z}{m_e^*} \tag{1.42}$$

1.2.2.1 Effect of magnetic field on the Density of States in 3D system

In the presence of strong magnetic field B_z, 3D allowed states of conduction electrons in *k*-space transform into a set of concentric tubes which is parallel to the applied magnetic field. As a result, each Landau level consists of degeneracy given by $g_n = \frac{eB}{\pi}$ [8]. Since, the

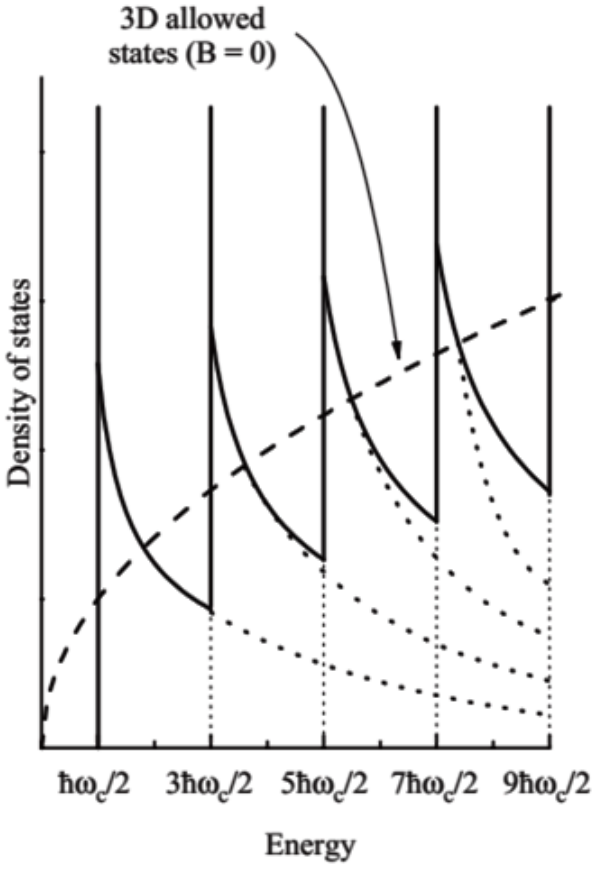

Fig.1.5 Schematic representation of Density of state vs. energy of electrons in 3D in presence of applied magnetic field [8]

conduction electrons are free to move in only one direction i.e. z – direction, hence each Landau level will show 1D free electron behavior along the direction of applied magnetic field B_z and hence the density of states (DOS) function will show the 1D DOS function form i.e. $g(E) \propto 1/\sqrt{E}$. Since there is singularities for the every Landau levels (n=1,2,3…) in the DOS function of 1D system at the bottom but due to the electron scattering phenomenon these singularities are removed (Fig. 1.5).

1.2.3 Effect of magnetic field in 2D systems

Let us consider a 2D system placed in xy plane and let z be the direction of applied magnetic field B_z, hence the force exerted by this magnetic field will be in the xy plane. As a result energy levels of conduction electrons are completely quantized and follow the 1D quantum harmonic oscillator model. The energy of such type of system may be expressed as

$$E_n = \left(n + \frac{1}{2}\right)\hbar\omega_c \text{ Where n=0, 1, 2, 3…..} \quad (1.43)$$

Here, $$\omega_c = \frac{eB_z}{m_e^*} \quad (1.44)$$

It is clear from the expression (1.43) that energy is quantized and it is completely dependent on quantum number n and applied magnetic field through cyclotron frequency (ω_c) [8].

1.2.3.1 Effect of magnetic field on the density of states in 2D system

Due to the application of external magnetic field, 2D system behaves as a 1D quantum harmonic oscillator hence for each Landau levels, DOS collapse into a δ–function. The energy of lowest Landau level is $\hbar\omega_c/2$. Ideally it should be delta function but practically electron suffers scattering during the motion in crystal as a result broadening occurs which is

shown in Fig.1.6. All the energy levels having an interval of $\hbar\omega_c$ collapse in the same Landau levels, degeneracy associated with each Landau levels may be expressed as $D = \frac{eB}{2\pi\hbar}$ [8].

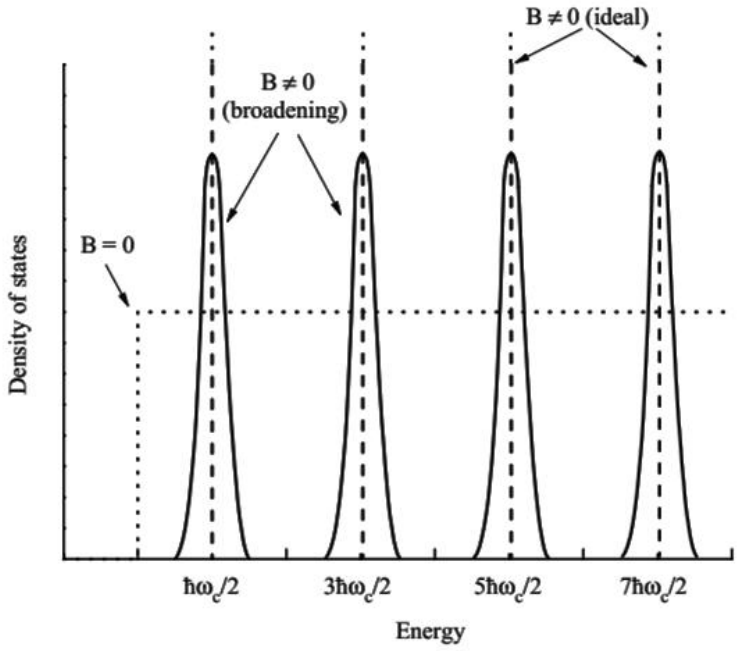

Fig.1.6 Schematic representation of Density of state vs. energy of 2D electron gas in presence of applied magnetic field [8].

1.2.4 Quantum Hall Effects (QHE)

At low temperature, when electrons confined to 2D are placed in high magnetic field, a series of steps in the Hall resistance as a function of magnetic field instead of the monotonic increase has been observed. In 1978, K. von Klitzing had seen such type of flat Hall plateaus; in 1985 he was also awarded Nobel Prize in Physics for the discovery of Quantum Hall effect. In 1980, the precise quantized value of the Hall resistance is given as

$$R_H = \frac{1}{n}\frac{h}{e^2} = 25812.807\Omega\frac{1}{n}, \text{ where n=1, 2, 3} \qquad (1.45)$$

Now a day's R_H is known as the von Klitzing constant [when n = 1 in Eq. (1.45)] and is written as R_K. It is obvious from the Fig.1.7 that the experimental curve show broad plateaus.

It is also very interesting to see that the "plateaus" in the values of ρ_{xy} appear precisely when ρ_{xx} becomes zero. Some important features in the Integer quantum Hall Effect (IQHE) has been mentioned below,

(1) High magnetic field is needed.

(2) Time reversal symmetry (TRS) is not preserved.

(3) Accuracy of the quantum value of the Hall conductance is extremely high, it is upto few parts per billion (ppb).

(4) Longitudinal resistivity (equivalently conductivity) vanishes. Due to this, bulk of the sample is a perfect insulator; but along the edges of the samples electrons can transport without dissipation hence edges will be conducting and the bulk will be insulating.

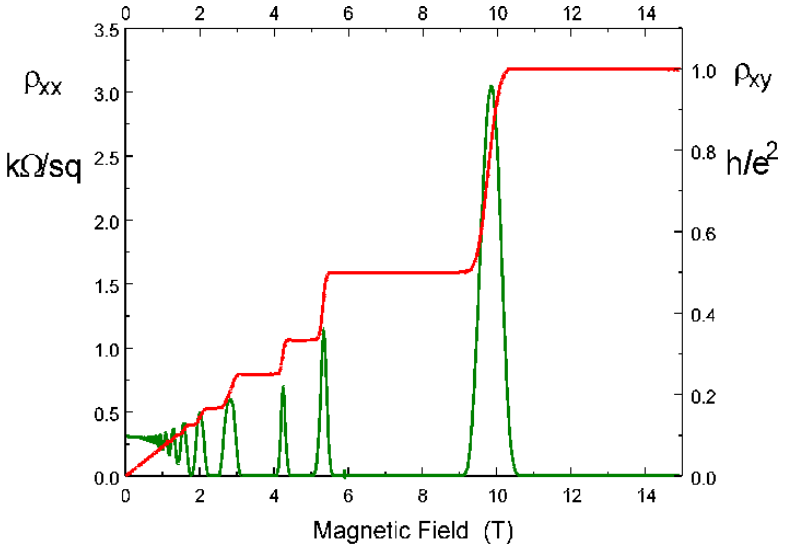

Fig.1.7 Schematic diagram of quantum Hall Effect, Adopted from (http://www.twinkletoesengineering.info /quantum_hall.htm).

1.2.4.1 Edge Sates

Let us consider a 2D system and the direction of applied magnetic field is perpendicular to this plane. Due to the effect of magnetic field, there will be formation of various landau levels correspond to different classical cyclotron orbits directed

counterclockwise (Fig. 1.8). These cyclotron orbits do not contain current but at the edges electrons move in “skipping orbits”and therefore a current so called “edge current” generates at the edges. The states associated with these skipping orbits are called “edge states”.The direction of propagation of electrons at the upper edge is opposite to the lower edge therefore the direction of edge current at the upper edge and lower edge will be opposite. As a result bulk of the material will be insulating due to the confined electron orbits but the edge will be conducting due to the skipping orbits. Since the direction of applied

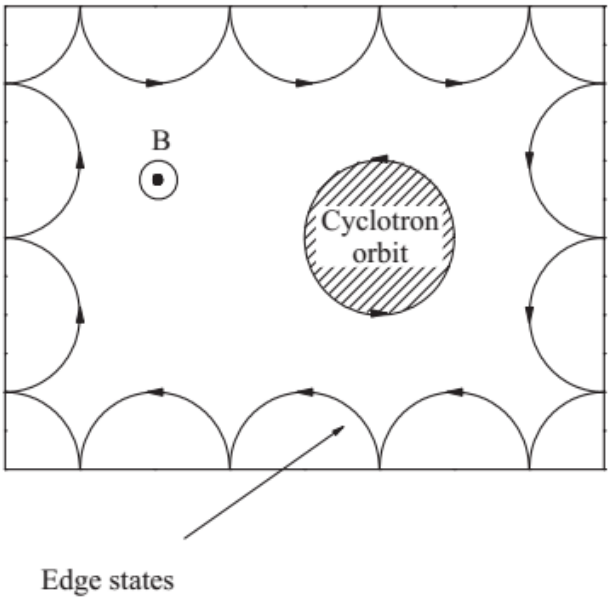

Fig.1.8 Cyclotron orbits (in the bulk) and skipping orbits (at the edges) in the 2D electron system in the presence of applied magnetic field [8].

magnetic field is fixed in a perpendicular direction to the plane (say along the positive z-direction), hence the direction of exerted force due to magnetic field will also be fixed. As a matter of fact, electrons will propagate in forward direction only, therefore there will be no effect of impurity on the propagation of these electrons therefore backscattering in such type of system is not possible. If we make a 3D system by stacking such type of 2D system by one

over one, the surface of that formed 3D system will be conducting but bulk will be insulating [8].

1.2.5 Quantum Spin Hall Effect (QSHE)

The quantum spin Hall Effect is another effect in topological insulators which is different from the quantum Hall effect. Unlike the quantum Hall Effect, no external magnetic field is required in the quantum spin Hall Effect and the currents are not necessarily quantized [9]. In fact, the required magnetic field is generated by the internal spin-orbit coupling. We have already discussed about quantization of transverse resistivity (ρ_{xy}) in quantum Hall effect, Lorentz force, due to which quantum Hall Effect generates, produces **A.p** term in the Hamiltonian. Now, the vector potential **A** in terms of symmetric gauge may be written as

$$A = \frac{B}{2}(y, -x, 0) \qquad (1.46)$$

Because of this, the Hamiltonian may be expressed as

$$H_{Lorentz}=C_1.\ B\ (xp_y\text{-}yp_x) \qquad (1.47)$$

Where C_1 is the proportionality constant term, p represents the momentum and A is the vector potential.

Berneviget. al. [3] argued for another force in nature which produces the similar Hamiltonian and that was the spin-orbit coupling force. The form of Hamiltonian turns to $(p\times E).\sigma$ where E is the electric field and σ is the Pauli spin matrix. Here instead of magnetic field B, electric field E has been used which preserve the time reversal symmetry. If the form of E is $E(\vec{x}+\vec{y})$ then the Hamiltonian becomes

$$H_{SO}=C_2.\ E\sigma_z(xp_y\text{-}yp_x) \qquad (1.48)$$

Here C_2 is proportionality constant, hence it is obvious from the equation that the opposite spin electrons will experience magnetic field directed in opposite direction. The up spin electrons would be chiral having a conductance quantized in fractional multiples of e^2/h, while the down spin electrons would be anti-chiral having a conductance in fractional multiples of $-e^2/h$.

In the quantum Hall Effect, the direction of motion of electrons in the upper edge and lower edge is opposite to each other. The left and right moving chiral edge states are spatially separated from each other (Fig. 1.8). They are protected from backscattering when exposed to impurities but in spin Hall Effect, each propagation channel of electrons are split into two. The top and bottom portion of the sample contain right as well as left moving electrons having up and down spin respectively [Fig.1.9(a and d)]. Backscattering of the electrons is still not allowed in quantum spin Hall Effect if nonmagnetic impurity is introduced. In fact, when a right-moving up spin electron backscatters from an impurity along a clockwise path, it suffers a phase difference π in this process and becomes a left-moving down spin electron. Similar phenomenon happens with the left- moving elections also. These two reflected wave functions interfere destructively with each other and therefore perfect transmission results. However, this scenario is only valid if left or right moving channels are odd in number. For example, if there were instead two right-moving and two left-moving channels: a right-moving up spin electron can then scatter into the left-moving up spin channel without picking up a phase difference, which allows it to interfere destructively. It is noteworthy that due to opposite chirality at the same edge time reversal symmetry is always preserved in quantum spin Hall Effect but if the impurity is magnetic then time-reversal symmetry (TRS) is no longer preserved. Due to this, perfect destructive interference is no longer possible and

backscattering would be allowed. The conduction electrons at the surfaces follow linear energy- momentum relation and therefore called as Dirac fermions. In 3D, it forms cone similar to graphene and that is called Dirac cone [shown in Fig. 1.9(e)]. Since the spins are polarized at the edges on 2D and on the surfaces in 3D TIs, therefore, the quantum spin Hall effect enables the realization of edge channel transport even in the absence of magnetic field and moreover the spin at the edge channels are polarized. One can utilize these spins for spintronics applications like spin-injection and detection, quantum computing and in dissipation less wire due to the absence of backscattering.

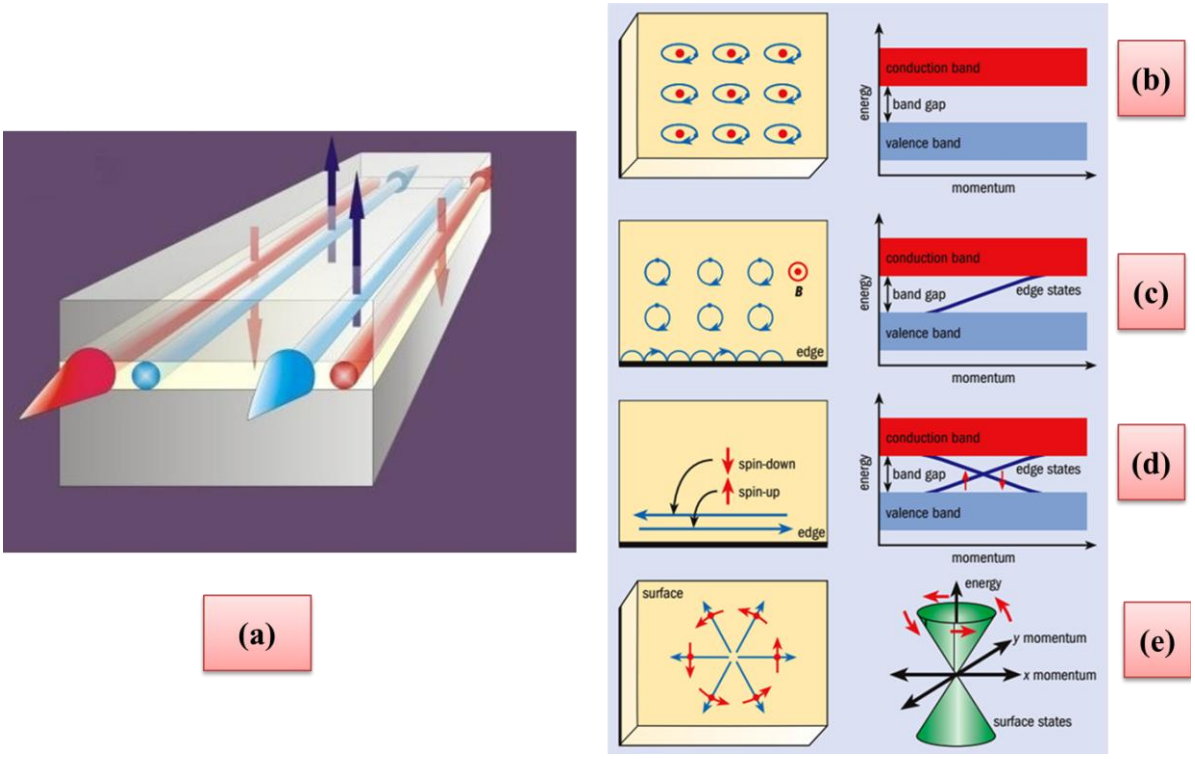

Fig.1.9 (a) Schematic diagram of quantum spin hall Effect, opposite spins propagating in opposite directions (b) Insulating state with a band gap seperating occupied and unoccupied state [9] (c) Bulk is insulating but skipping orbits at the edges permits the conduction of electron giving rise to the conducting edge i.e. zero band gap [9] (c) both type of left and right moving path having opposite spins is allowed in QSHE which is protected due to time reversal symmetry [9] (e) At the surface, propagation in any direction is possible, elecrons at the surfaces show linear energy momentum relation and hence show Dirac cone in 3D[9].

1.2.5.1 Spin Orbit Coupling (SOC)

When a charged particle moves in an electric field (E), the charge interacts with the electric field in momentum (p) dependent way. In the non-relativistic limit this interaction is described by a Hamiltonian or the spin-orbit interaction. If we start from the relativistic Dirac equation and pulling out the first corrections in the non-relativistic limit we will get the non-relativistic Schrodinger equation with some terms added. Among these extra terms there will be one term

$$H_{SO} = \frac{e\hbar\sigma.(E\times p)}{4m^2c^2} \tag{1.49}$$

Here H_{SO} is the Hamiltonian corresponds to spin orbit interaction; the above expression may also be expressed as

$$H_{SO} = -\frac{1}{2m^2c^2r}\frac{dV}{dr}S.L \tag{1.50}$$

Here S is the spin angular momentum and L is the orbital angular momentum vector.

1.2.6 Quantum Anomalous Hall Effect (QAHE)

If the material does not possess magnetic ordering, the Hall voltage is proportional to the applied magnetic field because it results from the deflection of charge carriers due to the Lorentz force. We can determine the Hall resistance defined as the developed transverse voltage divided by the current value. The slope of the curve shows linear field dependence and is governed by the type and density of carriers [Fig.1.10 (a)]. After the discovery of ordinary Hall Effect (OHE), Hall performed similar type of experiments on the materials having ferromagnetic ordering, but he found that the Hall resistance as a function of magnetic-field shows an unusual large slope at the low field [10]. Soon after, it was recognized that the origin of such type of unusual behavior is the magnetization of such

ferromagnetic materials, later it is known as the anomalous Hall Effect (AHE) [11]. Since a ferromagnetic material can show spontaneous magnetization even in the absence of external magnetic field, the anomalous Hall Effect can be measured in the absence of magnetic field also [Fig. 1.10(b]. Generally it is believed that the spin-orbit coupling plays a fundamental role in the origin of anomalous Hall Effect, but its exact origin is still not clear. One group recognized the impurity-induced skew-scattering or carrier's side jump as a reason for the anomalous Hall Effect, referred as a extrinsic mechanisms whereas the other thought that the anomalous Hall Effect originates from the property of the electronic energy band structures of ferromagnetic materials and is known as the intrinsic mechanism [11].We have already mentioned above that the anomalous Hall Effect in a materials having ferromagnetic ordering, can be induced by spontaneous magnetization even in the absence of external magnetic field [11]. Therefore, a quantized version of the anomalous Hall Effect named as the quantum anomalous Hall Effect (QAHE), indicates the realization of the quantum Hall Effect in the absence of magnetic field [11, 12]. After the discovery of the quantum anomalous Hall Effect, it was found that the theory which is applicable for the explanation in quantum Hall Effect may also be used to explain the phenomenon in anomalous Hall Effect in magnetic materials. The anomalous velocity which is used in the intrinsic anomalous Hall Effect is related to the Berry curvature of the energy band. The anomalous Hall conductivity of a material having magnetic ordering is also determined by the integral of the Berry curvature, but it is not quantized for a metal since the valence band is partly filled and hence the integral cannot be taken over the whole Brillion zone [11].

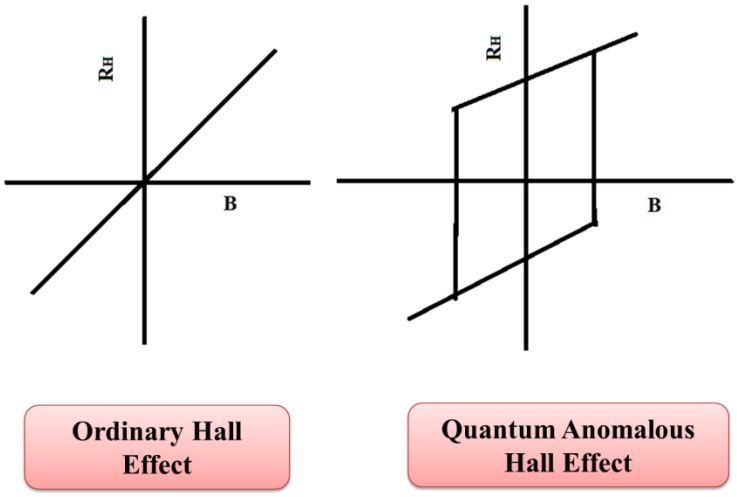

Fig.1.10 Schematic diagram of (a) ordinary Hall Effect (OHE) showing linear behavior between Hall coefficient vs. applied field (b) Quantum anomalous Hall Effect (QAHE) showing hysteresis in the graph of Hall coefficient vs. applied field.

1.2.7 Weak Antilocalization

Diffusion phenomenon is the dominating factor in transport experiment in the systems having low mobility and short mean free path. But in many semiconductors and in topological insulators also, phase coherence length is as long as from some nm to more than μm. Systems in which phase coherence length become comparable to the size of the sample, quantum interference phenomenon become an important factor in the correction of diffusion term. Materials having very low SOC or without SOC, quantum constructive interference phenomenon enhances the backscattering for the two time reversed (TR) scattering loops (Fig.1.11) as a result resistivity decreases i.e. conductivity increases. The quantum constructive interference phenomenon can be broken using external magnetic field. But tuning of quantum interference phenomenon from constructive to destructive has also been observed even in some materials having strong SOC, where due to the destructive

interference resistivity decreases and conductivity increases and weak antilocalization (WAL) takes place.

Not only the spin–orbit scattering but band structure with SOC can also leads to the WAL which can be explained on the basis of Berry phase. After an electron circled around Dirac point, the spin orientation of electron is rotated by 2π whereas its wave function is accumulated by π Berry phase. This π Berry phase tune the interference pattern of time reversed scattering loops from constructive to the destructive and therefore enhancement in conductivity results. This WAL effect can be destroyed using the magnetic field.

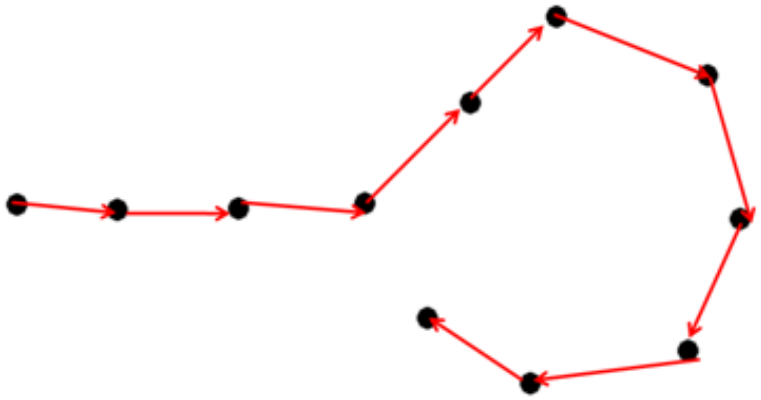

Fig.1.11 Schematic diagram of weak antilocalization (WAL), black dots represents the scattering centre and red lines are showing the direction of propagation of electrons.

1.2.8 Shubnikov-de Hass Oscillation (SdH) Oscillation

We have already discussed in QHE and QSHE that when we apply a strong magnetic field perpendicular to the plane of 2D electron gas, the energy levels split in to discrete levels called as Landau levels. As we increase the magnetic field, the separation between the Landau levels increases, therefore, position of the Landau levels varies with applied magnetic field, sometimes the landau level lies in between the Fermi energy level and electrons jump from occupied level (which is below to Fermi level) to unoccupied levels (which is above the

Fermi level), in this process electrons face scattering, as a result, a peak appears in the resistance vs. magnetic field graph, in the similar way when the levels do not lie in between the Fermi levels, electrons do not propagate hence no peak appears in R vs. B graph. Thus it is obvious that oscillations in resistivity called as Shubnikov-de Hass oscillation may be produced due to the variation in applied magnetic field. But if the direction of applied magnetic field is in plane of 2D gas, no oscillations in resistivity will appear, since no force will be exerted along the direction of field. Hence it is obvious that Shubnikov-de Haas oscillation only responds for the perpendicular magnetic field in 2D gas, therefore one cannot observe SdH oscillation for in-plane magnetic fields. But in 3D electron gas, SdH oscillation could be observed for magnetic field applied along any directions. Therefore we can use the angle dependence of SdH oscillation as a convenient tool to identify the dimension of carriers. Moreover, SdH oscillation revealed the coexistence of both three-dimensional bulk carriers with the two-dimensional surface states. Additionally, SdH oscillation also provides the information about the Berry phase. Zero Berry phase indicates about the normal fermions whereas π Berry phase shows the Dirac fermions present only on the surface of TIs.

1.3 Types of Topological Insulators

On the basis of properties, topological insulators may be classified in to two categories, 2D topological insulators and 3D topological insulators.

1.3.1 2D Topological Insulators

1.3.1.1 Graphene

In year 2005, a new state of matter called as Quantum-Spin-Hall insulator state [13] has been predicated by Kane and Mele. In this report they have discussed about the effect of spin orbit coupling on the band structure of graphene in the vicinity of Dirac point. There

was an inversion of band ordering at the K point with respect to K' point, inversion was different for opposite type of spins. Such type of band inversion leads to the quantum spin Hall Effect, in which at the edges, the movement of opposite spin electron is in the opposite direction which gives rise to the edge states. Unlike the quantum Hall Effect, time reversal symmetry (TRS) is preserved in quantum spin Hall Effect. Moreover edge state is protected

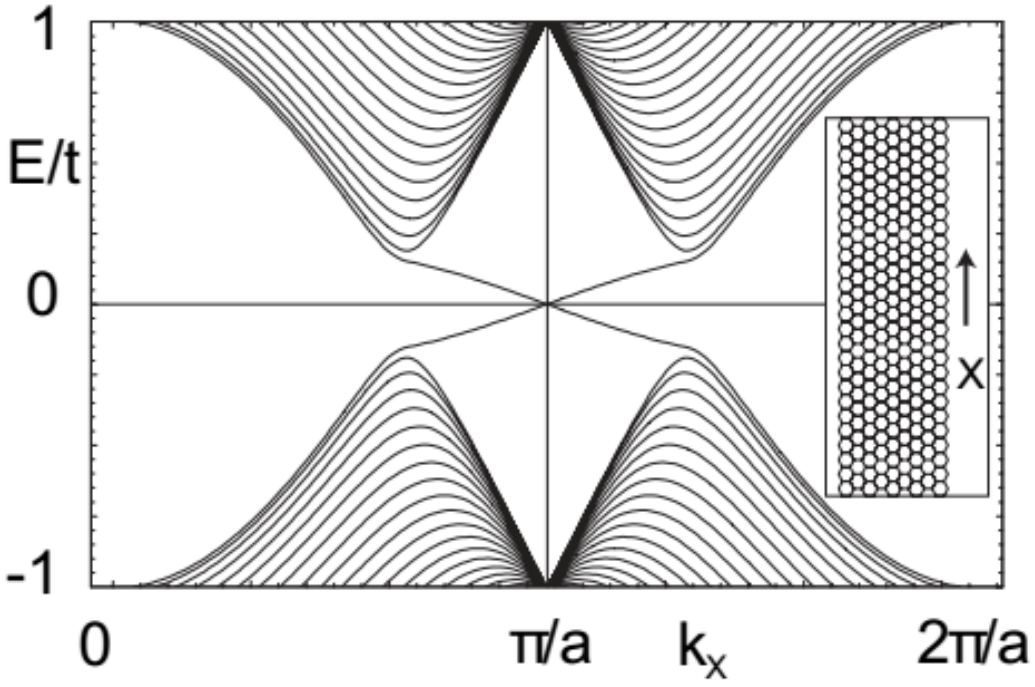

Fig.1.12 Band structure of Graphene at low energy introduced by Kane and Mele [13].

from backscattering but TRS can be broken using a magnetic field, as a result, backscattering becomes possible and hence the opening of band gap takes place. Kane and Mele [13] have reported the existence of quantum spin Hall Effect in the gap of graphene band structure (shown in Fig.1.12) and they mentioned that the quantum spin insulating behavior was different from the ordinary insulating behavior due to the topological order. But the predicted band gap in such type of system was as small as 10^{-3} eV [13]. The observation of such small band gap is only possible at very low temperature which is nearer to the order of mK or even

less than this. Moreover, such type of low band gap can be only observed if the quality of the sample is very near to the perfect sample. All these conditions could be fulfilled neither in sample nor in experiments which prevents the experimental observation of Quantum spin Hall Effect in graphene.

1.3.1.2 CdTe/HgTe/CdTe System

In 2006, Bernevig have reported about the thin layer of HgTe having thickness d_{HgTe} sandwiched between the two thin layers of CdTe with equal thickness d_{CdTe} [shown in Fig. 1.13(a)]. The band structure of this heterostructure depends on the thickness of HgTe. Such type of experiment led the discovery of quantum spin Hall Effect and the edge states in CdTe/HgTe/CdTe quantum wells [3]. It was expected that the electronic band structure of the quantum well of this heterostructure at the Γ point, mostly looks like HgTe which has an inverted band structure. But when the value of d_{HgTe} decreases, confinement energy increases, as a result, energy band shifts. When the value of d_{HgTe} becomes less than a critical value d_c~6.3 nm, the energy bands start to align, the nature of quantum well will be dominated by the properties of CdTe. When the value of d achieves the critical value, i.e. $d=d_c$, quantum spin Hall Effect appears even in the absence of external magnetic field. At the boundaries of two dimension quantum well, one dimension helical edge state appears and the band inversion takes place. The band structure of HgTe, CdTe and CdTe/HgTe/CdTe heterostructure has been shown in Fig. 1.13(b). Solid line indicates about Sketch of the band structure in CdTe/HgTe/CdTe quantum wells with the variation of the width'd' of the quantum well. Solid lines show the bulk bands and the dashed lines indicate about the energy bands within the quantum well. There is difference of some confinement energy between the energy of bulk band and

quantum well. It is also clear from the Fig. 1.13(b) that band inversion is taking place after a critical width d_c.

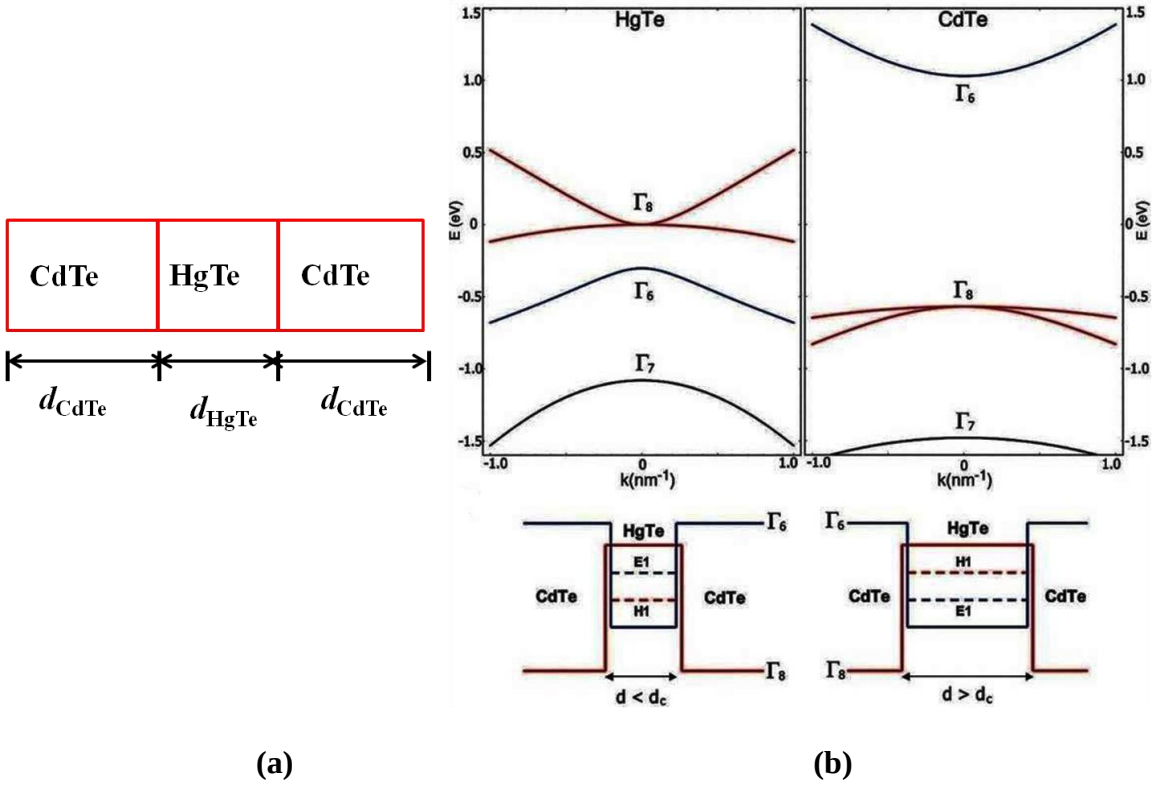

Fig.1.13 (a) Schematic diagram for CdTe/HgTe/CdTe heterostructure (b) Upper Figure showing bulk energy bands for HgTe and CdTe at Γ point, lower Figure showing CdTe/HgTe/CdTe quantum well in normal regime $d<d_c$ and in inverted regime $d>d_c$ [3].

At the boundaries of two dimension quantum well one dimension helical edge state appears and the band inversion takes place. At the critical thickness of 6.3nm, band gap vanishes and the Dirac cone touches each other at a point called Dirac point which we have already discussed in quantum spin Hall Effect section. The size of the band gap in such type of system was 40 meV which makes it possible in experimental observation. The experimental observation of the quantum spin Hall Effect in HgTe quantum wells system has been shown in the early days [14] which was followed by the some other experimental verification [15] in

the quantum spin Hall regime. Moreover the discovery of experimental evidence for the spin polarization of the quantum spin Hall edge states [16] also support this fact.

1.3.1.3 InAs/ GaSb System

Soon after the experimental observation of quantum spin Hall Effect in CdTe/HgTe/CdTe quantum well, it was predicted that when Fermi level lies inside the band gap, QSHE may also exist in type II semiconductor such as InAs/Gasb/AlSb [17]. The condition is similar to the previous case in CdTe/HgTe/CdTe system. In Fig.1.14 quantum well structure of InAs/Gasb/AlSb has been shown, it is obvious from the Figure that the valence band edge of GaSb is located at 0.15 eV higher than that of the conduction band edge of the InAs layer, here layers of AlSb serve as the confining outer barriers. Hole subbands are localized in the GaSb layer, whereas electron subbands are localized in the InAs layer. We will mainly focus on the lowest electron subband E1 which is s type and hole subband H1 which is p type heavy hole bands. If the thickness of the quantum well decreases, the E1 band edge decreases and H1 band increases in energy. At the critical thickness $d=d_c$, crossing of the band occurs and the level of E1 located downside than that of the H1 and hence the inversion takes place. As a result of spin orbit coupling and band hybridization of E1 and H1 bands, a small gap exists at the crossing points of the original bands and hence the system has a bulk band gap with gapless linearly dispersive edge state. According to the report of Liu et al. [17], if the thickness of GaSb layer is fixed at 10 nm then at the critical thickness 9nm of InAs, a crossing at K point occurs between the E1 and H1 band. Such type of crossing indicates about the phase transition of the sample from normal insulator to the quantum spin Hall insulator.

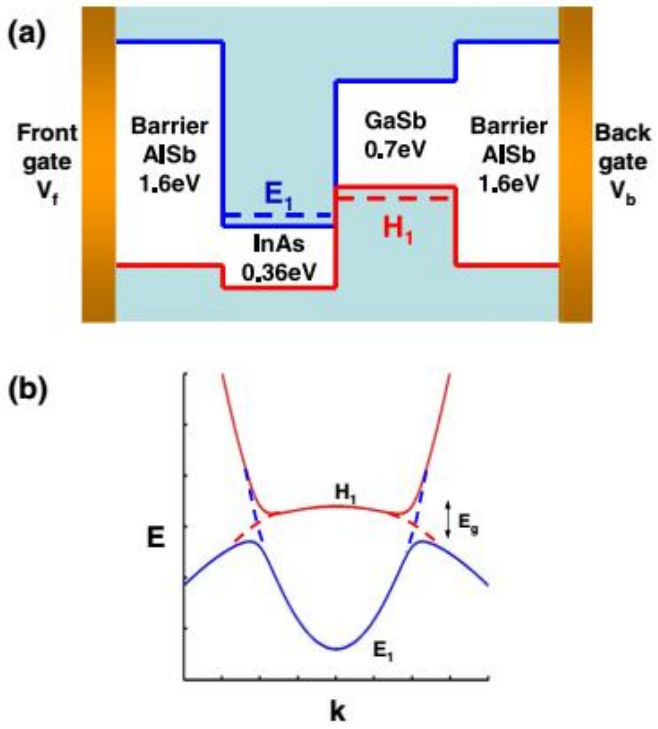

Fig.1.14 (a) Band gap and band offset diagram for asymmetric AlSb/InAs/GaSb quantum wells. The left AlSb barrier layer is connected to a front gate while the right barrier is connected to a back gate. The E_1 subband is localized in the InAs layer and H_1 is localized in the GaSb layer. Outer AlSb barriers provide an overall confining potential for electron and hole states. (b) Schematic band structure diagram. The dashed line shows the crossing of E_1 and H_1 in the inverted regime. Hybridization between E_1 and H_1 opens the gap [17].

1.3.2 3D Topological Insulators

By the generalization of concept of 2D topological insulator, one can develop the concept of 3D topological insulator. Moore and Balents [18], Roy [19] and Fu, Kane and Mele [20], established the concept of 3D topological insulators. In 2D topological system only edges are conducting whereas in 3D topological system entire surface of the material is conducting. The band structure of surface state in 3D TIs can be characterized as a 2D state with the band dispersion of a single Dirac cone. The surface state of strong TIs contains odd number [1] of Dirac cones. In 3D TIs, there are four Z_2 topological invariants (ν_0; ν_1 ν_2 ν_3), here ν_0 is the strong topological invariant and ν_1-ν_3 is the weak topological invariant. The topological state ν_0=1 leads to the odd number of gapless topological surface state present in

all of the surfaces of the topological material. The important property of 3D topological insulators is locking of spin and momentum in the perpendicular direction on the surfaces of 3D TIs. The state having momentum k and –k have opposite spins i.e. if up spins are propagating in positive x direction then only negative x direction is available for the negative spins hence surface of 3D topological insulators is robust against back scattering (shown in QSHE section 1.2.5). Hasan et al. [1] mentioned that time reversal symmetry (TRS) is always preserved at the surface of 3D TIs; as a consequence back scattering of electrons at the surfaces by 180^0 is not possible.

On the basis of the robustness of the surface against back scattering, we can also categorize the 3D topological insulators in weak and strong topological insulators.

1.3.2.1 Weak Topological Insulators

SnTe was the first material which has inverted band structure. In SnTe and PbTe conduction band and valence band edge occurs at the L point in Brillouin zone. In SnTe, conduction band edge is located at L_6^+ and valence band edge is at L_6^- but the condition is opposite in PbTe, where conduction band edge is located at L_6^- and valence band edge is at L_6^+ (Fig. 1.15), hence one can apply topological engineering here. When we increase the Sn concentration in $Pb_xSn_{1-x}Te$, L_6^+ level will rise up and L_6^- will go down and at a certain concentration these two bands will touch each other and the zero band gap condition takes place [21].

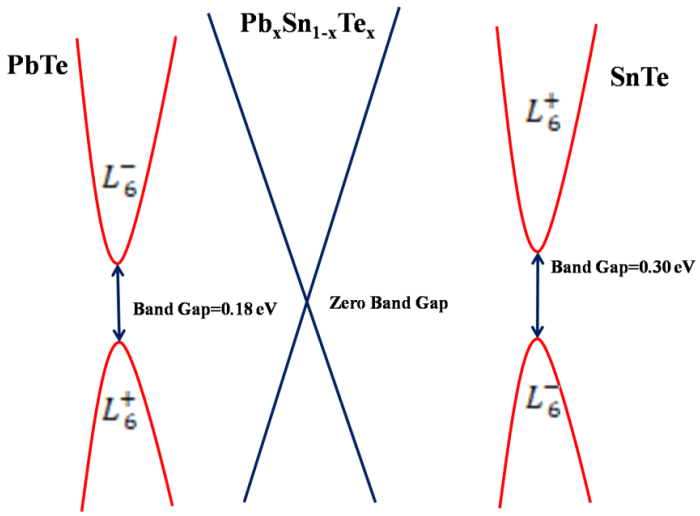

Fig.1.15 Schematic diagram for valence band and conduction band for SnTe and PbTe materials.

1.3.2.2 Strong Topological Insulator

1.3.2.2.1 The First 3D Topological Insulator $Bi_{1-x}Sb_x$

Hsieh et al.in 2008 [22] showed the first experimental proof for the existence of 3D topological insulator state in the material $Bi_{1-x}Sb_x$. The band structure of $Bi_{1-x}Sb_x$ has been studied using the angle-resolved photoemission spectroscopy (ARPES) technique.

Both pure Bi and Sb are semimetal character having finite band gap. It is clear from the Fig. 1.16 that there is a difference in the band ordering at the L- point in both of the materials. In Bi, valence band symmetry is L_a and the conduction band symmetry is L_s which is inverted in the case of Sb, where L_s is the valence band symmetry and L_a is the conduction band symmetry (Fig. 1.16). Therefore, if we combine these two materials, topological engineering can be applied. Using ARPES study, Hsieh et al. [22] have found a set of surface state in $Bi_{0.9}Sb_{0.1}$ system which crosses the Fermi energy five times. Such type of odd number of crossings indicates about the topologically protected states in $Bi_{0.9}Sb_{0.1}$.

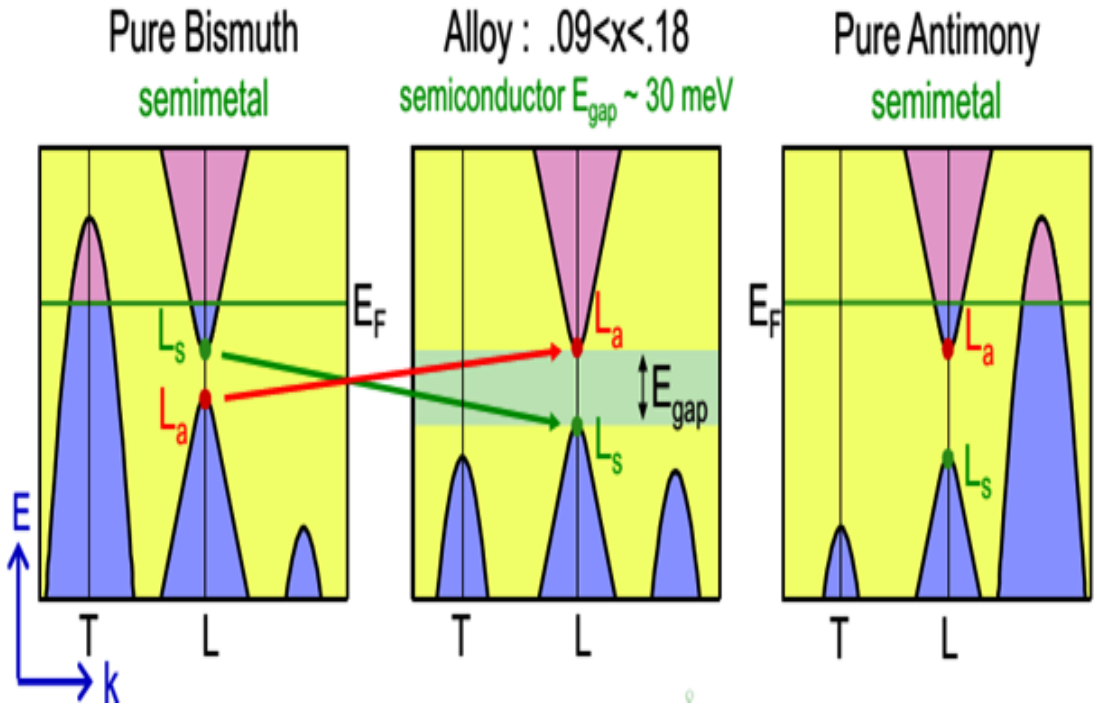

Fig.1.16 Schematic diagram for the valence band and conduction band for pure Bi, Sb and $Bi_{1-x}Sb_x$. Adapted from Hasan et al. [1].

But major challenge was to separate out the bulk and insulating contribution as bulk is insulating and surface is conducting in TIs. This issue can be solved using ARPES, which is an ideal technique to probe the surface characteristic of topological insulator. Using this technique, we can distinguish the surface and bulk properties of the 3D TIs, since there is no dispersion in the surface state along the perpendicular direction but the bulk state do. Besides these interesting features, ARPES can be used in spin resolution mode also [Fig. 1.17(a)]. Using this mode we can not only estimate the spin orientation on the Fermi surface but also get information about the Berry phase and spin momentum locking which is the peculiar property of the surface in TIs [1, 22, 23, 24].

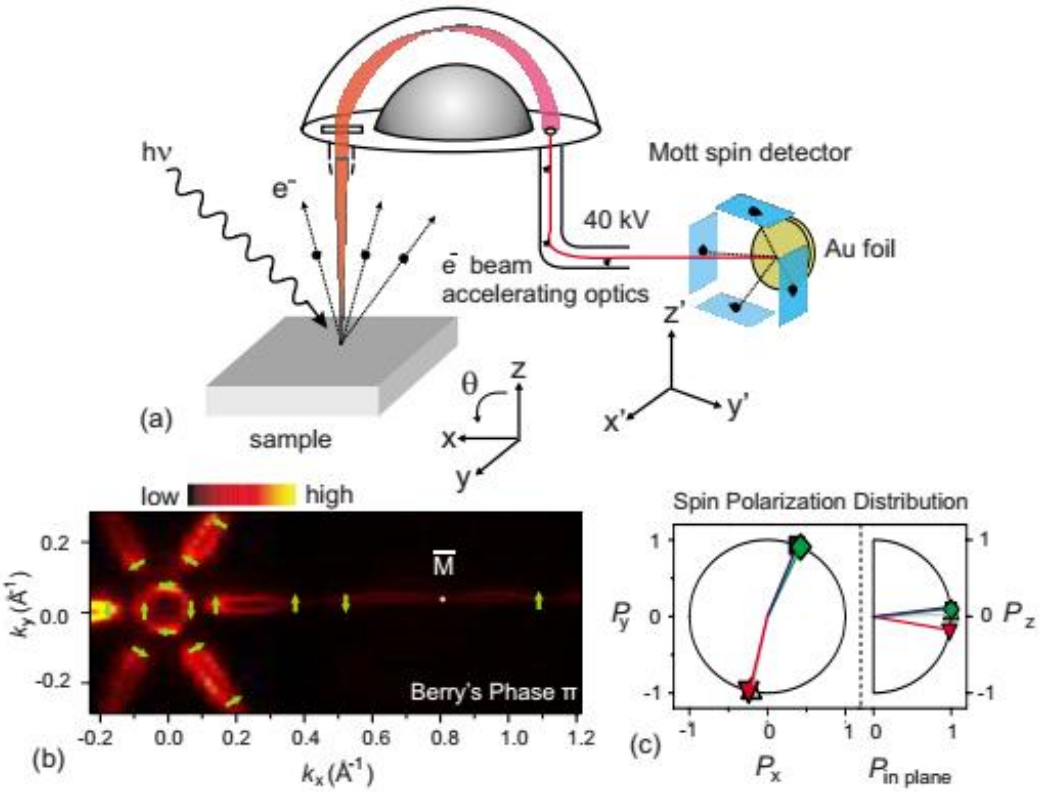

Fig.1.17 Spin resolved ARPES study of the topological insulator surface. (a) Schematic diagram of spin-ARPES measurement setup which was used to measure the spin distribution on the (111) surface Fermi surface of the sample $Bi_{0.91}Sb_{0.09}$. (b) Spin orientations on the surface create a vortex like pattern around Γ point. A net Berry phase is extracted from the full Fermi-surface data. [1, 22] (c) Net polarizations along *x*, *y*, and *z* directions are shown. P_z~0 suggests that spins lie mostly within the surface plane. Adapted from [1, 23, 24].

Hsieh et al. [22, 23, 24] have experimentally reported the surface and bulk electronic structures of the $Bi_{0.09}Sb_{0.91}$ using the ARPES spectra. Fig. 1.18 represents the variation of energy of the occupied states with momentum along the line which connect the $\bar{M}$ point to $\bar{\Gamma}$ in the Brillouin zone. The surface band crosses the Fermi energy five times (Fig. 1.18). This odd no of crossing indicates about the topologically protected surface of the material. Moreover, using the spin resolved ARPES technique Hsieh et al. [1, 22, 23, 24] have shown the spin polarization on the surface of the $Bi_{0.09}Sb_{0.91}$ (Fig. 1.17), they have shown the first direct evidence of the π Berry phase. They have also estimated that the spin polarization rotates around 360^0 around the central Fermi surface which is shown in Fig. 1.17(c) [1, 22, 23, 24].

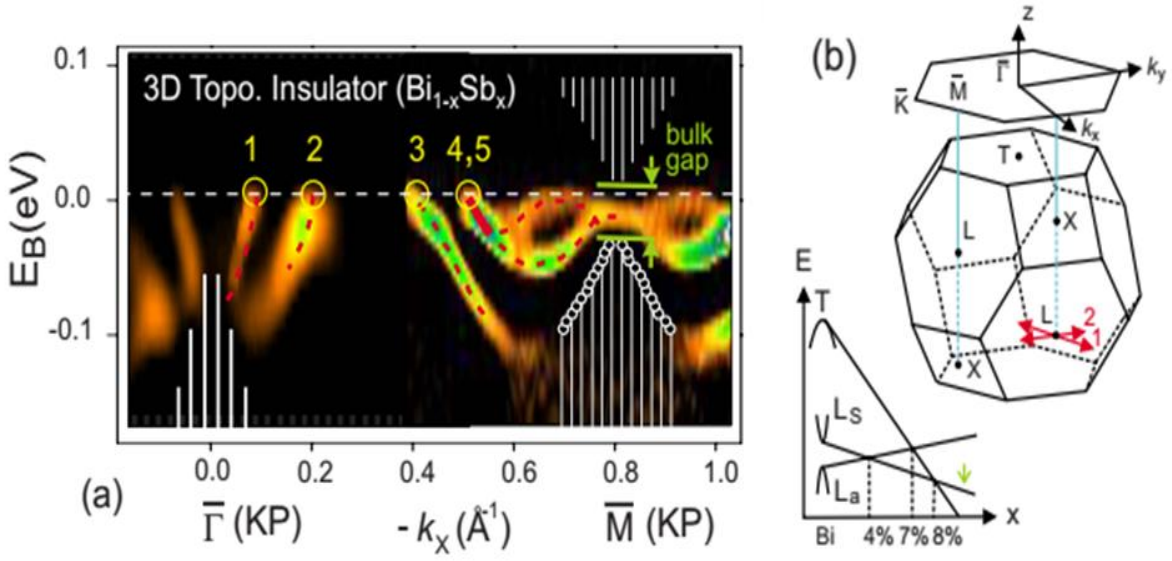

Fig.1.18(a) ARPES study of $Bi_{1-x}Sb_x$ on the (111) surface of $Bi_{0.9}Sb_{0.1}$ which probes the occupied surface states as a function of momentum on the line connecting the time reversal invariant points $\bar{\Gamma}$ and $\bar{M}$ in the surface Brillouin zone. Only the surface bands cross the Fermi energy five times. (b) A schematic diagram of the 3D Brillouin zone and its (111) surface projection. Adapted from Hasan et al. [1] Hsieh et al. [22].

Using STM and ARPES analysis, Roushan et al. [25] argued the absence of backscattering at the 2D surface state in TIs. It has been already discussed that due to the TRS, backscattering is prohibited at the surface of 3D TIs. $Bi_{0.92}Sb_{0.08}$ has been studied using the scanning tunneling spectroscopy (STS). Spatially resolved conductance maps of the (111) surface over an area 1000Å×1000Å for $Bi_{0.92}Sb_{0.08}$ has been shown in Fig. 1.19(a), whereas Fig. 1.19(b) is showing the spin-ARPES map of the surface at the Fermi level. Arrow are showing the direction of spins. Fourier transform scanning tunneling spectroscopy (FT-STS) has been shown in Fig. 1.19[(c), (d) and (e)] which represent the joint density of states (JDOS) computed from Fermi surface with and without suppression of k to –k backscattering. The similarity between Fig. 1.19(d) and (e) is indicating about the absence of backscattering for k to –k [1, 24, 25].

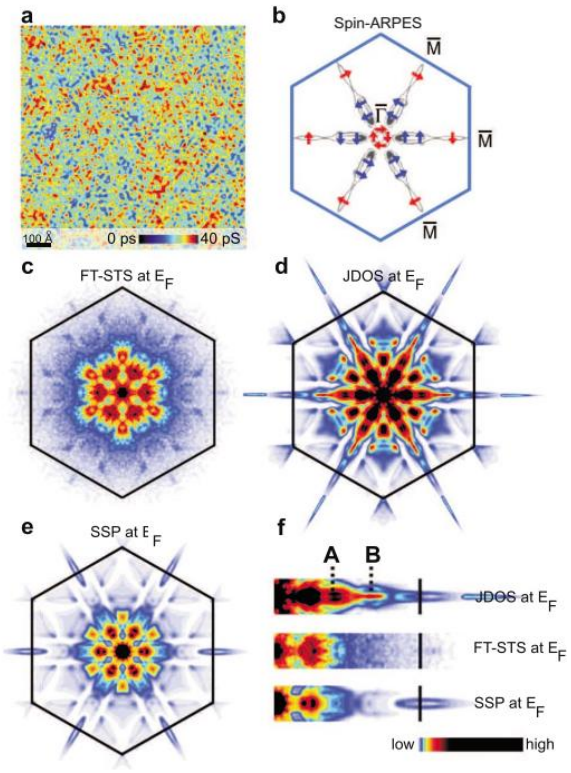

Fig.1.19(a) Spatially resolved conductance study of the (111) surface obtained at 0 mV over an scanning area of 1000Å×1000 Å. (b) Spin-ARPES study of the surface state measured at the Fermi level. Arrows are showing about the spin textures from spin ARPES measurements. (c) Fourier transform scanning tunneling spectroscopy FT-STS at Fermi energy (E_F). (d) The joint density of states (JDOS) at Fermi energy (E_F). (e) The spin dependent scattering probability (SSP) at Fermi energy (E_F). (f) Close up of the JDOS, FT-STS and SSP at Fermi energy (E_F), along the Γ-*M* direction. Adapted from [1, 24, 25].

1.3.2.2.2 New Materials Bi_2Te_3, Bi_2Se_3 and Sb_2Te_3

In 2009 Zhang et al. [26] have reported some other 3D topological insulators Sb_2Te_3, Bi_2Te_3 and Bi_2Se_3 having a large band gap in bulk and single Dirac cone on the surfaces. *ab initio* functional theory has been used for the calculation [26]. Non-trivial surface states in Sb_2Te_3, Bi_2Te_3 and Bi_2Se_3 have been shown in Fig. 1.20. The order of calculated band gap was ~ 100 meV for Bi_2Te_3 material and ~300 meV for Bi_2Se_3 materials. Since Bi_2Se_3, Bi_2Te_3 and Sb_2Te_3 have the same strong topological invariant as $Bi_{1-x}Sb_x$, therefore various studies have been done on these TIs [26-34]. Moreover, unlike the $Bi_{1-x}Sb_x$ which is an alloy, these compounds are pure hence in principle these materials can be prepared up to high purity.

Additionally surface state of these TIs can be observed easily in ARPES study (shown in next section), finally these TIs has a large band gap (Bi_2Se_3~0.3 eV, Bi_2Te_3~0.10 eV and Sb_2Te_3~0.26 eV) which can be observed at room temperature. Hence all these facts indicate that Sb_2Te_3, Bi_2Te_3 and Bi_2Se_3 materials can exhibit topological behavior even at room temperature (300K).

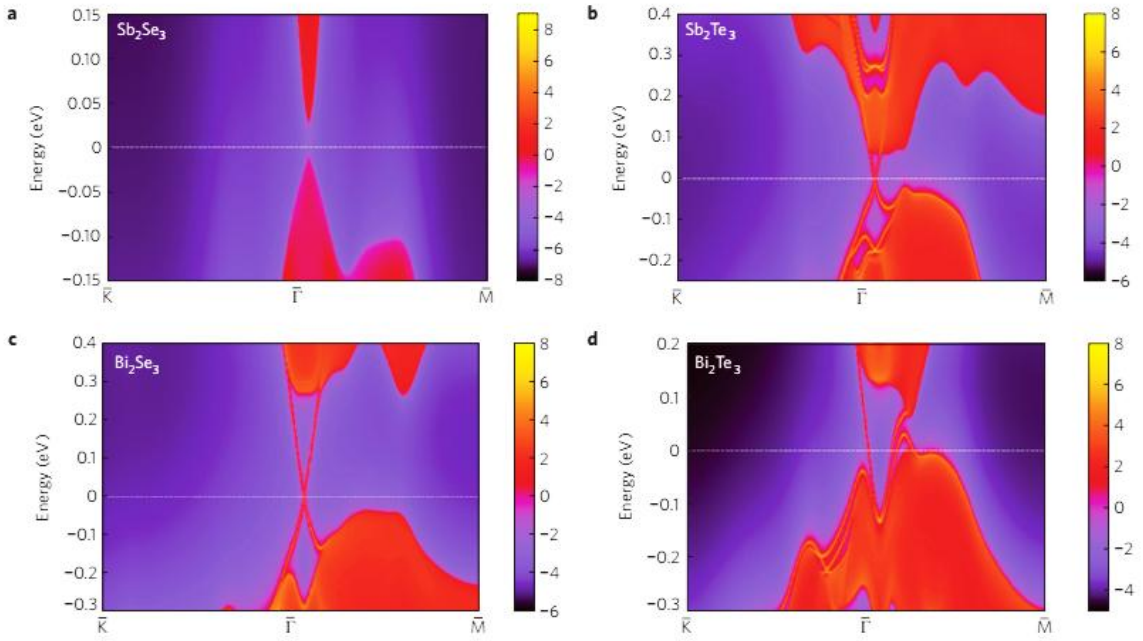

Fig.1.20 Band structure of Sb_2Se_3, Sb_2Te_3, Bi_2Se_3 and Sb_2Te_3 calculated by *ab initio* density functional theory, red represents occupied bulk and surface states and blue the bulk band gap**.** Adapted from Zhang et al. [26].

1.3.2.2.2.1 Crystal Structure and Symmetry Properties

Bi_2Te_3, Sb_2Te_3 and Bi_2Se_3 types of materials have layered rhombohedral crystal structure with D_{3d}^5(R-3m) space group. Crystal structure of Bi_2Se_3 has been shown in Fig. 1.21. It is obvious from the Figure that the structure consists of quintuple layers arranged in Se1-Bi-Se2-Bi-Se1 sequence along the c axis. Such type of structure is often known as the tetradymite- type lattice. There is covalent bonding within a layer and weak van der Waals interactions between the layers. The thickness of one quintuple layer is 1nm. Crystal

structure consists of two Bi and three Se atoms in a unit cell in which two equivalent Bi atoms (Bi and Bi'), two equivalent Se atoms (Se and Se') and one in-equivalent Se atom from Se and Se' i.e.Se2 exist [27].

Each atomic layer forms a triangle lattice. For every layer, there are three possible positions A, B and C along the *z* direction. The triangle layers are stacked in the order A-B-C-A-B-C- along the z-direction [Fig. 1.21(c)]. For example if Se atom is occupying A position in a quintuple layer, it cannot occupy the same position i.e. A position in the next quintuple layer, it can occupy only B or C position. In Fig. 1.21(a), crystal structure of Bi_2Se_3 has been shown, position of Se2 atom is taken as the position of origin, The direction of z axis is perpendicular to the plane of layer, x axis is along the binary axis having two fold rotation symmetry, the direction of y axis is taken along the bisectrix axis, which is the crossing line of the reflection plane and the atomic layer plane of Se2. As for as we consider the symmetry of such type of crystals, there are four types of symmetries present in the crystals [27]

1- **Threefold rotation R3 along the z –direction**: Such type of symmetry can be created due to the following transformation:

   $x \rightarrow x\cos\theta - y\sin\theta$, $x \rightarrow x\sin\theta + y\cos\theta$ and $z=z$ where $\theta=2\pi/3$

2- **Two fold rotation R2 along the x -direction**: Such type of symmetry can be generated by the following transformation Bi1→Bi', Se1→Se' and Se2→Se2 with the coordinate transformation $x \rightarrow x$, $y \rightarrow -y$ and $z \rightarrow -z$. Under this transformation the layers Bi1 (Se1) and Bi1' (Se1') interchange their positions.

3- **Inversion P. P**: In the inversion symmetry Bi1→Bi1, and Se1→Se1'; Se2→Se2 takes place whereas coordinates changes by, $x \rightarrow -x$, $y \rightarrow -y$ and $z \rightarrow -z$. The site containing

Se2 is the inversion center of such type of structure; hence we can take Se2 as the point of origin. Under inversion operation, Bi1 (Se1) changes in to Bi1' (Se1').

4- **Time reversal T**: Such type of operation is given by T=ΘK, where T represent time operator, K is the complex conjugate operator and $\Theta=i\sigma_2$, where σ is the Pauli matrix for spins.

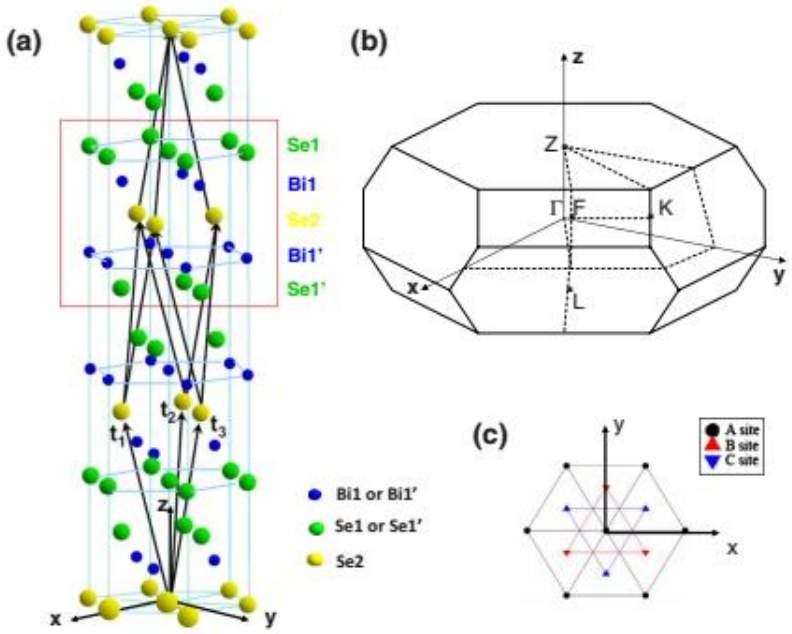

Fig.1.21 (a) Crystal structure of Bi_2Se_3 (b) Brillouin zone of Bi_2Se_3 (c) Three possible positions A, B, C in-plane triangle lattice. Adapted from Liu et al.[27].

1.3.2.2.2.2 Band Inversion in Bi_2Se_3 System

In Bi_2Se_3 system, the outermost shells of both Bi and Se are p orbitals. The outermost configuration of Bi and Se atoms are $6S^2\ 6p^3$ and $4S^2\ 4p^4$ respectively. Since in a unit cell there is five atoms, two Bi and three Se and the outermost cell of each atoms contain three p orbitals p_x, p_y and p_z, hence there will be total fifteen p orbitals in a unit shell of Bi_2Se_3. Let us introduce these orbitals as $|\Lambda, \alpha>$ where Λ= Bi, Bi', Se1, Se' and Se2 and $\alpha=p_x$, p_y and p_z. Since Se1 and Se1' layers are situated at the outmost in the cell and Se layer lies in between

the Bi1 and Bi1' layers hence coupling between Se layer and Bi layer is strongest. Due to the chemical bonding hybridization, Bi energy levels are pushed up and Se levels are pushed down (shown in I step of Fig. 1.22). In II step parity has been considered. According to parity Bi energy level splits in to two levels (one odd, one even) $|B_\alpha>$ and $|B_\alpha'>$, whereas Se energy levels split in to three states (two odd and one even) $|S_\alpha>$, $|S_\alpha'>$ and $|S0_\alpha>$. Hence total five levels will be there. Now, due to the inversion symmetry bonding and anti-bonding states can be given as

$$\left|P1^{\pm},\alpha\right\rangle = \frac{1}{\sqrt{2}}\left(\left|B_\alpha\right\rangle \mp \left|B'_\alpha\right\rangle\right), \qquad \text{For Bi atoms} \qquad (1.51)$$

$$\left|P2^{\pm},\alpha\right\rangle = \frac{1}{\sqrt{2}}\left(\left|S_\alpha\right\rangle \mp \left|S'_\alpha\right\rangle\right), \qquad \text{For Se atoms} \qquad (1.52)$$

The upper index indicates about the parity. The energy of anti-bonding states is higher than that of bonding energy states [27]. The energy levels $P1^{+}_{x,y,z}$ and $P2^{-}_{x,y,z}$ is found to be nearer to the Fermi energy. So we will consider these orbitals only. Crystal field theory comes in to existence in the III step shown in Fig.1.22. According to the crystal field theory, P_z orbitals have different energy than the P_x and P_y orbitals and these two orbitals remain degenerate. Now $P1^{+}_{z}$ and $P2^{-}_{z}$ remain closer to the Fermi level. At the IV stage when spin orbit coupling (SOC) takes place, $(P2^{-}_{+}, \pm\frac{1}{2})$ energy levels goes up and $(P1^{+}_{-}, \pm\frac{1}{2})$ goes down (Fig.1.22), hence it is clear that due to the spin orbit coupling the energy level which is below to the Fermi level goes upside and the level which is above to the Fermi level goes down therefore spin orbit coupling is the deciding factor for the band inversion in Bi_2Se_3 system. Thus we can say that due to the strong SOC, the opposite parity states got inverted and drive the system in to topological insulator phase, which is similar to the phenomenon in 2D HgTe system. Same type of analyses can be used for the 3D topological insulators such as Bi_2Te_3

and Sb_2Te_3 system but in Sb_2Te_3 system SOC is not sufficiently strong to invert the energy levels.

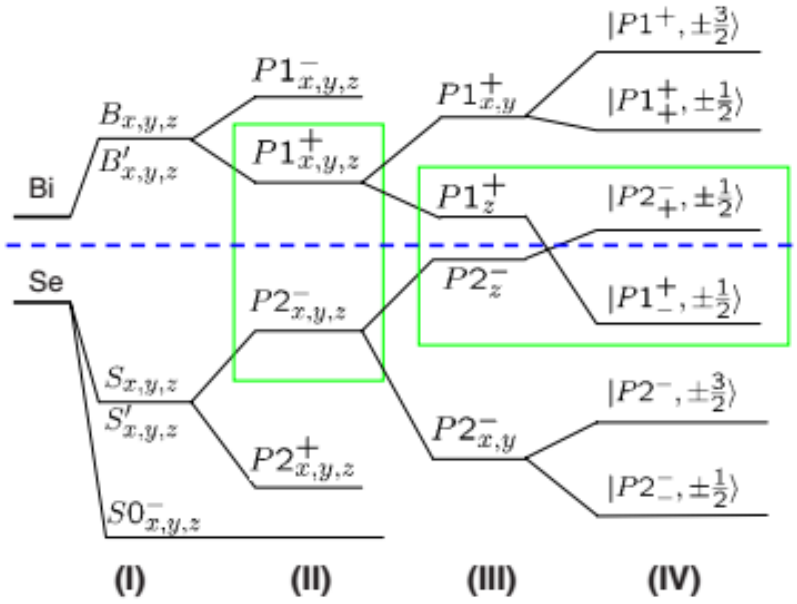

Fig.1.22 Schematic representation of the band structure of Bi_2Se_3(I) Hybridization of Bi and Se orbitals (II) formation of bonding and anti bonding states due to inversion symmetry (III) Crystal field splitting (IV) effect of spin orbit coupling. Adapted from Liu et al.[27].

1.3.2.2.2.3 ARPES Study

This prediction about Bi_2Se_3 has been further confirmed by Xia et al. [28] and Chen et al. [5]. Using the ARPES technique, Xia et al. studied Bi_2Se_3 system (Fig 1.23 and Fig. 1.24). Fig. 1.23 is clearly showing that the surface states are linearly dispersed and are located ~0.3 eV below than the Fermi energy level. The quadratically dispersed bulk state is very close to the Fermi level and it is located ~0.1 eV below the Fermi level. The extended states from -0.3 eV downwards are attributed to the onset of the valence bands. Energy dependent scans have been performed in order to differentiate the surface and bulk states since bulk states disperse while no change occurs in the surface state (Fig. 1.23). Single polarized Dirac cone in Bi_2Se_3 system has been shown in Fig. 1.24(a). The bulk and surface states are clearly observed shown by shaded regions and line respectively [Fig. 1.24(c].

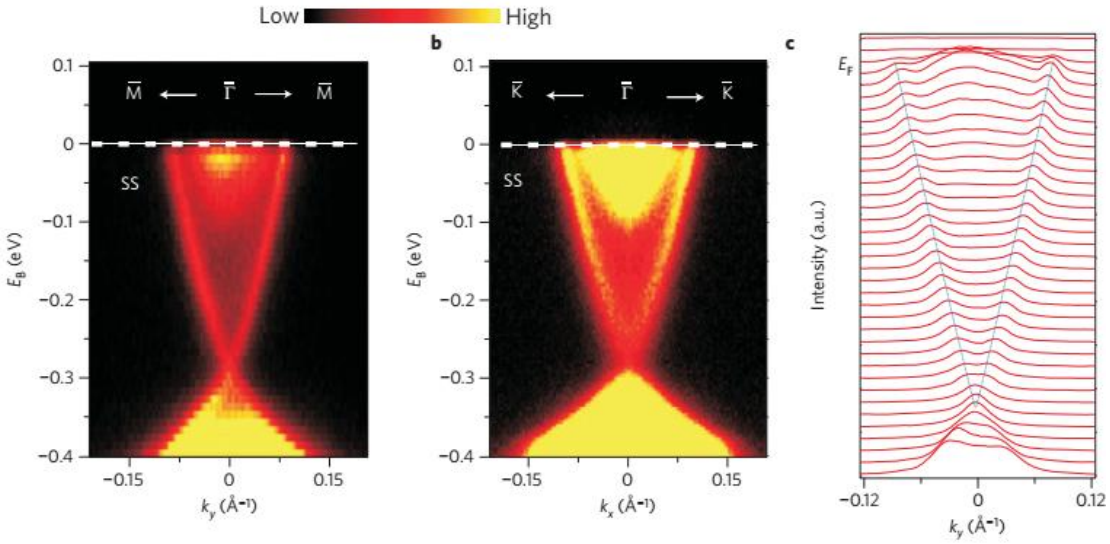

Fig.1.23 ARPES measurement of Bi_2Se_3 (a, b) cuts along the M-Γ-M and K-Γ-K directions (c) momentum distribution curve corresponding to (a) [28].

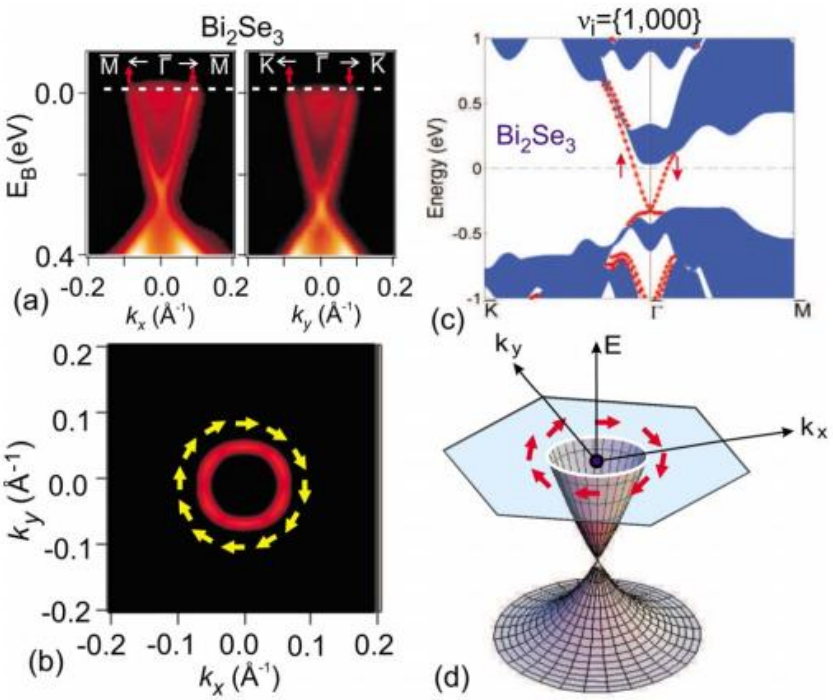

Fig.1.24 (a) ARPES study of Bi_2Se_3 showing surface electronic states with a single spin polarized Dirac cone. (b) The surface Fermi surface exhibits a chiral left handed spin texture. (c) Surface electronic structure of Bi_2Se_3 computed in the local density approximation. The shaded regions describe bulk states and the lines are showing the surface states. (d) Schematic of the spin-polarized surface-state dispersion in Bi_2X_3 (1;000) topological insulators. Adapted from Xia et al.[1, 23, 28, 29].

Chen et al. [5] have studied the behavior of the band structure of Bi_2Te_3 sample with the varying concentration of Sn (Fig. 1.25). It was clear from the study that all of the samples were showing the topological surface state (shown in the (ii) row) with gapped bulk state. The constant energy cut [shown in row (i)] indicates about the hexagonal distortion in K in the surface states in Bi_2Te_3 sample. This type of distortion from a perfect linear dispersed state is called as hexagonal warping and this is because of the interaction between surface and bulk states. It is clear from the Fig. 1.25 that Chen et al. [5] were successful to shift the Fermi energy in the bulk band gap by using the different doping concentrations of Sn in to Bi_2Te_3.

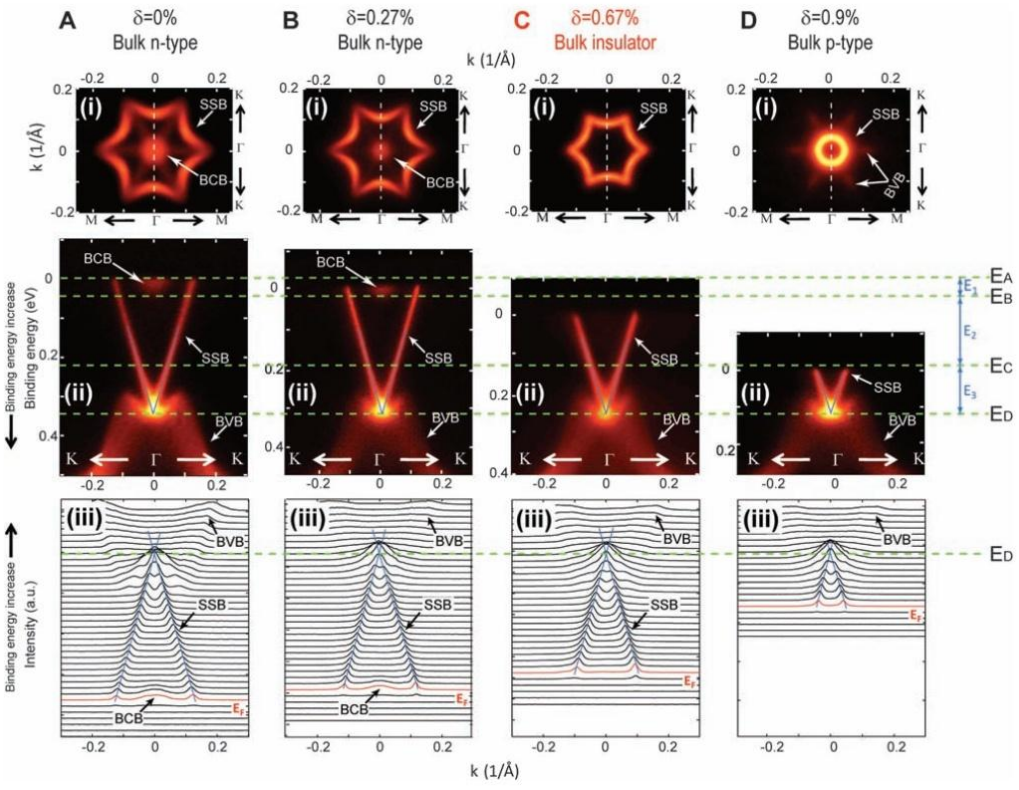

Fig.1.25 ARPES experiment of Bi_2Te_3 topological insulator, A to D is presenting the result of doping concentration Sn in to Bi_2Te_3 from δ=0 to 0.9%. Each section is showing the band dispersion along the K-Γ-K direction and the respective momentum distribution curve, here SSB stands for surface state band, BCB- bulk conduction band and BVB- bulk valence band. Adapted from Chen et al.[5].

Surface of the TIs are protected by TRS which is unaffected from non magnetic impurities. Dirac cone touches each other at a point called as a Dirac point and there is no band gap at the surface [shown in Fig.1.26 (a)], but if we introduce magnetic impurity such as Fe, Mn, Ni etc., then breaking of TRS takes place at the surfaces of TIs as a matter of fact the two branches of Dirac cone separated out from each other hence gap opening at the Dirac point results [Fig.1.26 (a)] [1, 23, 29, 30]. In fact, there is interaction between Fe ions and Se surface which generate the 'time reversal symmetry breaking disorder potential' on the surface. When non magnetic disorder was created by the absorbent of NO_2 or alkali element Li, K or Na in Bi_2Se_3 and Bi_2Te_3 system, Dirac cone still intacted with each other. The result was consistent with the fact that the TRS is robust against the nonmagnetic disorder at the surfaces[shown in Fig.1.26(c and d)].

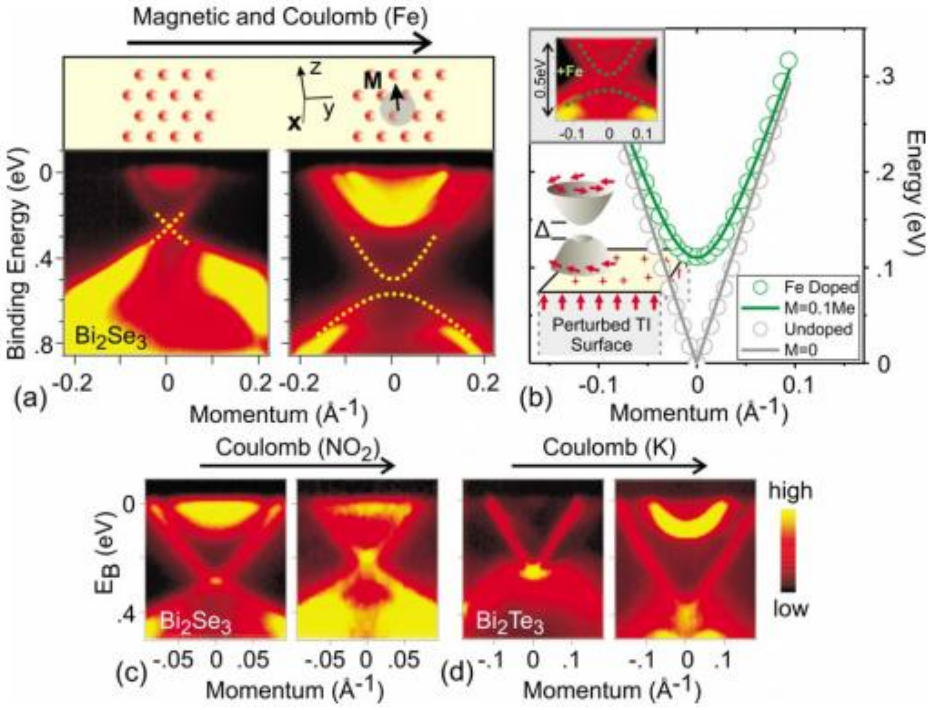

Fig.1.26 Magnetic impurity such as Fe on the surface of Bi_2Se_3 opens a gap at the Dirac point. The interaction of Fe ions with the Se surface set a band gap and the time reversal symmetry breaking disorder potential introduced on the surface. (b) A comparison of surface band dispersion with and without Fe doping. (C) and (d) Nonmagnetic disorder created via molecular absorbent NO_2 or alkali atom adsorption K or Na on the surface leaves the Dirac node intact in both Bi_2Se_3 and Bi_2Te_3. Adapted from [1, 23, 28].

1.3.2.2.2.4 Magnetic and Transport Properties

Various studies have been done on the magnetic and transport properties of topological insulators using electrical resistivity, Hall experiment, magnetoresistance (MR) and Thermoelectric measurements. [31-34]. Tuning of the carrier type may also be very important for the application point of view by using different type of materials in series. Jo et al. have studied the effect of Fe in magnetic and transport properties of the $Bi_{2-x}Fe_xTe_3$ (x=0, 0.08, 0.15, 0.20, 0.25 and 0.30). Tuning of carrier from n type to p type has been observed in $Bi_{2-x}Fe_xTe_3$ with x=0.30 [31]. Diamagnetic state up to x=0.025 and paramagnetic state at the doping concentration of x=0.30 has been found [Fig. 1.27(a)] and Curie temperature was below 12K. Moreover, metallic behavior up to x=0.25 sample has been observed but for the sample x=0.30, semiconducting behavior has been seen up to 150K and above this temperature sample was again metallic [Fig. 1.27(b)].

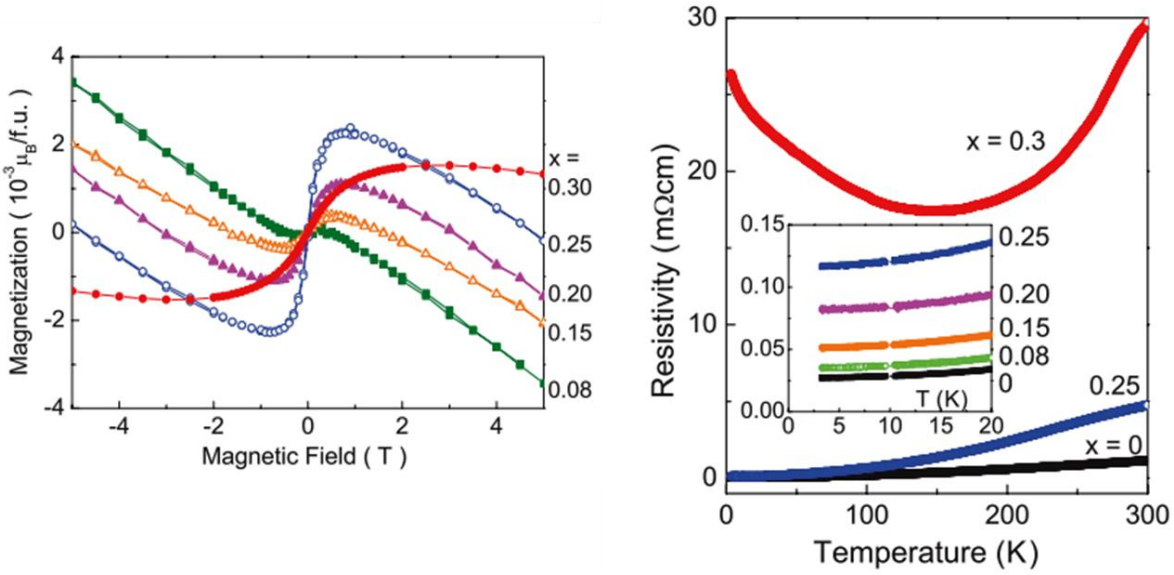

Fig.1.27 Variation of Magnetization vs. applied magnetic field for samples $Bi_{2-x}Fe_xTe_3$ (x=0, 0.08, 0.15, 0.20, 0.25 and 0.30) (b) variation of electrical resistivity vs. temperature for samples $Bi_{2-x}Fe_xTe_3$ (x=0, 0.08, 0.15, 0.20, 0.25 and 0.30), Inset shows the zoom picture of resistivity below 20K [31].

Choi et al. [32] have also mentioned the tuning of carriers from n to p type in $Bi_{2-x}Mn_xSe_3$ (x=0, 0.03, 0.05, 0.09 and 0.15) samples. Behavior of carriers was n type below 5% concentration of Mn but it was p type above this concentration. Electrical resistivity as a function of temperature was showing metallic behavior for x< 0.05 but it was showing upturn towards lower temperature side for x≥0.05 [shown in Fig. 1.28(a)].

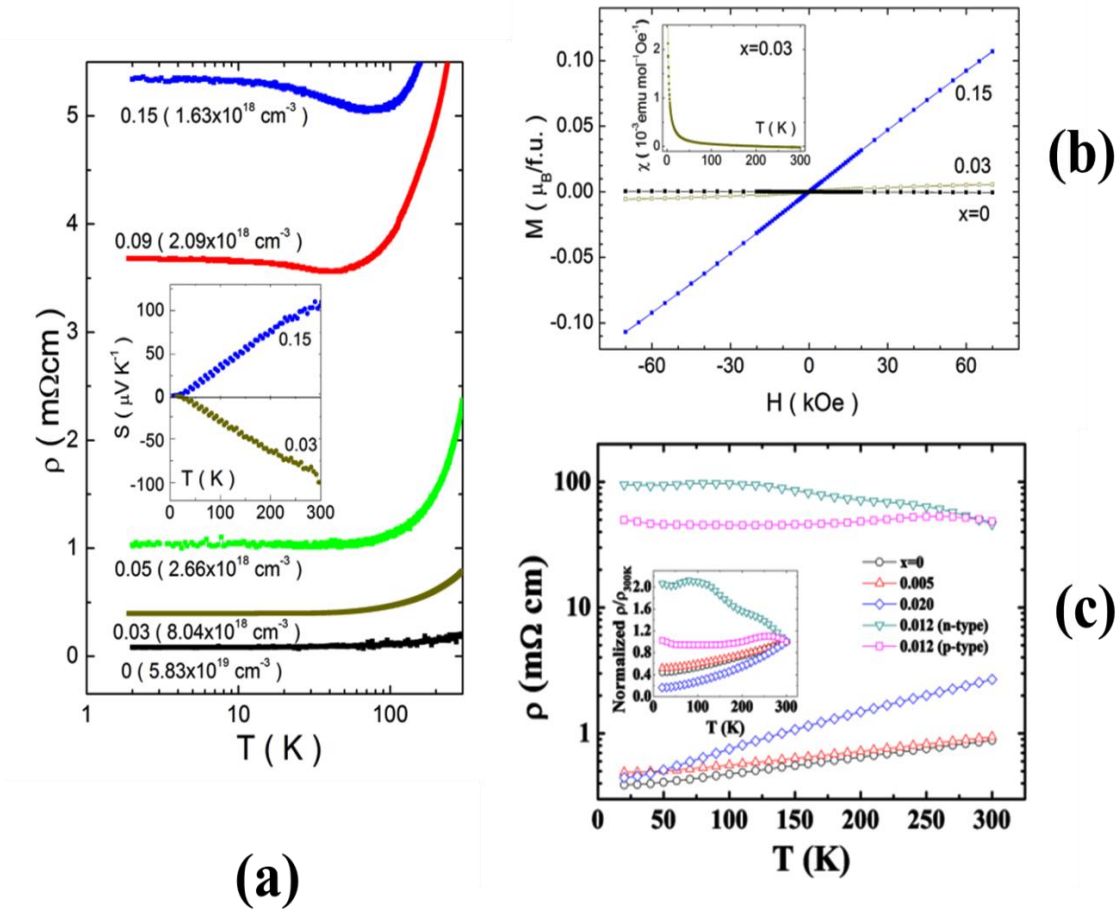

Fig.1.28 (a) Variation of electrical resistivity vs. temperature for samples $Bi_{2-x}Mn_xTe_3$ (x=0, 0.03, 0.05, 0.09 and 0.15), Inset shows the seebeck coefficient of sample (x=0.03 and 0.15) [32] (b) Variation of Magnetization vs. applied magnetic field for samples x=0.03 and 0.15, Inset represents the χ vs. T graph for x=0.03 sample [32] (c) Variation of electrical resistivity vs. temperature for samples $Bi_{2-x}Ca_xSe_3$ (x=0, 0.005 and 0.012) , Inset shows the normalized resistivity [33].

Thermoelectric properties have been also measured and the maximum value of Seebeck coefficient (S) has been found to be 100μV/K but the absolute value of S was same for both n and p type of samples [Inset of Fig. 1.28(a)]. As far as the magnetic properties is

concerned, sample was showing diamagnetic behavior for x=0 sample and above this concentration sample was paramagnetic [Fig. 1.28(b)]. Similar type of crossover in carriers has been also found in the report of Wang et al. [33], where they have used $Bi_{2-x}Ca_xSe_3$ (x=0, 0.005, 0.012, 0.015 and 0.020) samples [Fig. 1.28(c)]. It is clear from the graph that sample was showing metallic behavior at x=0, 0.005 and 0.020 while sample x=0.012 was showing insulating behavior. They have explained this drastic change on the basis of variation in the carrier density as a function of temperature.

Magnetoresistance (MR) behavior in different systems has been studied by various groups [34-39]. Wang et al. [34] found giant linear magnetoresistance (GLMR) behavior in Bi_2Te_3 nanosheets and they have predicted quantum origin of this GLMR [Fig. 1.29(a)]. For the explanation of the origin of the GLMR, Abrikosov [35] proposed a quantum model. This model can be applied for the materials having zero band gap and linear Dirac dispersion. In this model, it is predicted that nonstoichiometry induced disorder transfer the gapped materials into zero gap with a Dirac cone like linear energy spectrum. According to this model under 'extreme quantum limit' only one Landau level with a linear energy spectrum get populated by all of the conduction electrons and only this Landau level participate in conductivity. The quantum MR should be positive, linear down to very small field, nonsaturating and independent of temperature. Abrikosov has also predicted that the fluctuation in mobility is caused by disorder which is responsible for the linear magnetoresistance. On the basis of random resistance network Parish and Littlewood [36] have proposed another model for the explanation of LMR, in this model it is believed that the fluctuation in the mobility rather than the disorder is the key factor for the origin of LMR.

This model also predicts that dMR(T) should proportional to μ(T) where μ is the mobility [Fig. 1.29 (b and c)] [36].

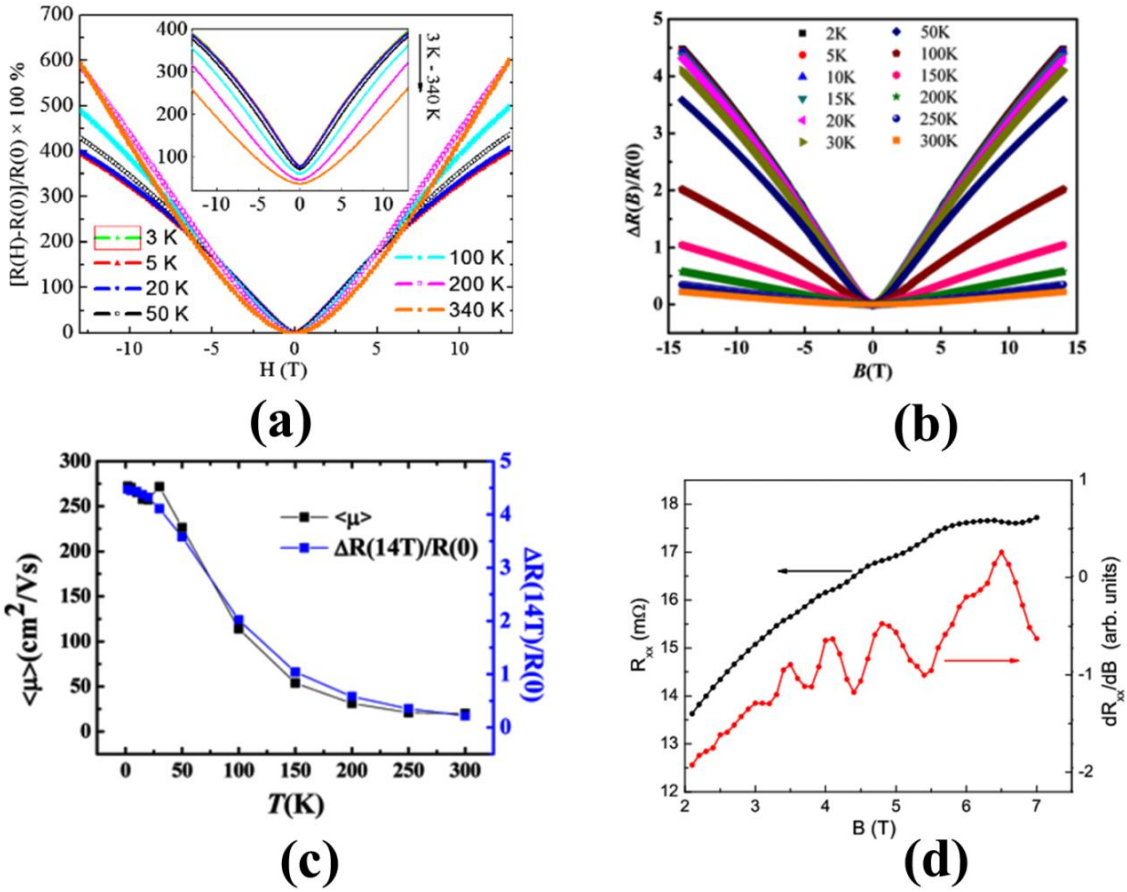

Fig.1.29 (a) Variation of MR as a function of applied magnetic field (H); Inset shows the MR ratio between 3K-340K for Bi_2Te_3 nanosheets (b) Variation of MR as a function of applied magnetic field showing linear behavior in Bi_2Te_3 film (c) Plot of Hall mobility and MR showing good agreement with PL model in Bi_2Te_3 film (d) SdH oscillations in $Bi_2Se_{2.1}Te_{0.9}$.

Oscillation in longitudinal resistivity in presence of magnetic field called as Subnikov-de Haas (SdH) oscillation, is an important tool to prove the surface state in topological insulators. Various studies have been done based on this interesting phenomenon [Fig 1.29(d)] [37-39]. Such type of oscillations can be observed in very good quality crystals, at low temperatures and in high magnetic fields. SdH oscillations are one of the much effective tools to investigate the topology of the Fermi surface of both bulk and surface

which is a fundamental key for the study of the physical properties in the metals [38]. The measurement accuracy in the determination of Fermi surface cross-sectional areas is better than 0.1% of the area of the Brillouin zone whereas in case of effective mass accuracy is better than ~5% [39].

Various interesting studies have been done to establish the superconducting phase in TIs, hydrostatic pressure is applied for the presence of superconductivity phase in pure Bi_2Te_3 [40-42]. According to the report of K. Matsubayashi [40], at the pressure near 8GPa

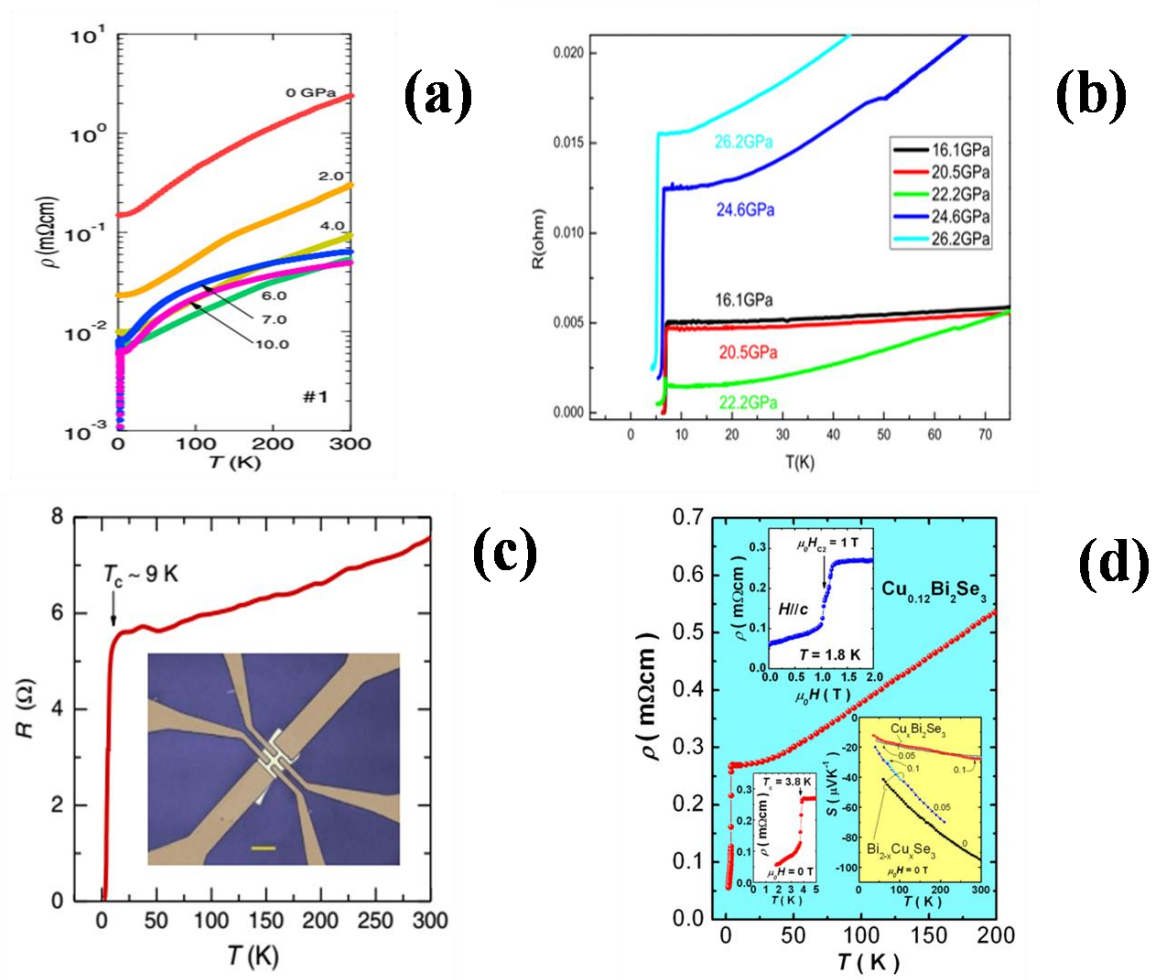

Fig.1.30 (a) Variation of resistivity vs. temperature for Bi_2Te_3 sample showing superconductivity (Tc)~ 2.7K [40] (b) Variation of resistivity vs. temperature for Bi_2Te_3 sample showing superconductivity (Tc)~ 8K [41] (c) Variation of resistivity vs. temperature for Bi_2Te_3 sample showing superconductivity (Tc)~ 9K [42] (d) Variation of resistivity vs. temperature for $Cu_{0.12}Bi_2Se_3$ sample showing superconductivity (Tc)~ 3.8K [43].

the maximum obtained superconducting critical temperature (Tc) was 2.7K [Fig. 1.30(a)] whereas relatively higher critical temperature (Tc) was observed by Zhang et al. [41], they have applied 30GPa pressure on pure Bi_2Te_3 sample and the maximum achieved Tc was around 8K [Fig. 1.30(b)], moreover another group have also found superconducting phase in pure Sb_2Te_3 [42] at ambient pressure and relatively high temperature ~9K [Fig.1.30(c)]. Instead of using pressure Hor et al. [43] used intercalation of Cu to get superconducting phase in Bi_2Se_3 and T_c was 3.8K which was lower than the earlier mentioned T_c. [Fig. 1.30(d)].

Due to the ease in preparation, large observable bulk band gap, Dirac cone on the surfaces, interesting transport and magnetic properties, the materials Bi_2Te_3, Sb_2Te_3 and Bi_2Se_3 are the most researched 3D topological insulators now a days. We will mainly focus on the magnetic and magneto-transport properties of Bi_2Te_3 and Sb_2Te_3 topological insulators.